DEVICE-INDUCED ERYTHROCYTE DEFORMATION USING M-FLOW VISUALIZATION

by

Rui Zhao

BS, Tianjin University, 2001

Submitted to the Graduate Faculty of

School of Engineering in partial fulfillment

of the requirements for the degree of

Master of Science

University of Pittsburgh

2004

UNIVERSITY OF PITTSBURGH

SCHOOL OF ENGINEERING

This thesis was presented

by

Rui Zhao

It was defended on

December 2, 2004

and approved by

Marina V. Kameneva, Ph. D., Associate Professor
Department of Bioengineering

Zhongjun Wu, Ph. D., Assistant Professor
Department of Surgery
University of Maryland School of Medicine

Anne M. Robertson, Ph. D., Associate Professor
Department of Mechanical Engineering

Thesis Director: James F. Antaki, Ph. D., Associate Professor
Department of Bioengineering

© Rui Zhao, 2004

DEVICE-INDUCED ERYTHROCYTE DEFORMATION USING M-FLOW VISUALIZATION

Rui Zhao, MS

University of Pittsburgh, 2004

Implantable cardiovascular devices are commonly used in clinical treatment for end stage cardiovascular devices. However, they may cause device-induced blood damage which can cause serious complications such as hemolysis and thrombosis. Blood damage often occurs within small passages or journals of the flow path. These regions may be associated with hot-spots in which shear stress is excessive and cells may be irreversibly strained. The successful design of these devices relies on efficiently minimizing supra-physiologic shear fields through computational modeling. However the fundamental blood mechanics under these conditions are not yet fully characterized.

This study was therefore conducted to elucidate the microscopic mechanics of cellular deformation that underlie shear-induced hemolysis. A micro fluid system was developed to emulate flow environments at hot-spots and provide optical access for microscopic visualization. The flow of red blood cells (RBCs) within micro channels was illuminated by a pair of stroboscopes resulting in a rapid succession of images -- recorded by double-exposure digital CCD camera. Red blood cell motion and deformation dynamics, as well as the surrounding fluid velocity field under various conditions of hematocrit, flow rate were quantitatively measured using particle image velocimetry (PIV) technique.

The results show that cells deform rapidly as they approach the inlet, bear the largest deformation at inlet, keep large deformation inside channel and recover as soon as flowing out of exit. Inside channel, cell deformation will reach to a threshold that the cells will not be elongated as shear stress increases. We concluded that the largest possibility for blood damage occurs at the inlet of gaps or clearance in cardiovascular devices, due to the combined effect of extensional stress and shear stress. The combined effect is great on blood mechanical damage in that it can deform the cell to a maximal value in a transient time. The sublethal damage is more likely to happen than the visible rupture of red cells in our experimental situation.

Our findings show basic mechanism underlining device-induced blood damage. The methods are proved to be effective and ready to be applied in further design and investigations.

TABLE OF CONTENTS

ACKNOWLEDGEMENT xiii

1.0 INTRODUCTION 1

1.1 BLOOD AND BLOOD DAMAGE 1

1.1.1 Blood and blood rheology 1

1.1.1.1 Macroscopic RBC rheology 1

1.1.1.2 Microscopic observation of RBC rheology 2

1.1.2 Blood cell damage 3

1.1.2.1 Previous studies for RBCs damage 4

1.2 DEVICE INDUCED BLOOD DAMAGE 5

1.2.1 Cardiovascular devices 5

1.2.2 Hemolysis induced by implantation, clinical reports 5

1.2.3 Sublethal blood damage 6

1.2.4 Previous attempts on design and optimization 6

1.3 MOTIVATION 9

1.4 AIM OF THESIS 9

2.0 METHODS 11

2.1 SAMPLE PREPARATION 11

2.1.1 Low viscosity blood sample 11

2.1.2 High viscosity blood sample 12

2.2 MICRO-FLUID SYSTEM 12

2.2.1 Micro channel design and fabrication 15
2.2.1.1 Coordinate system 15
2.2.1.2 Channel dimension design 16
2.2.1.3 Mask design 20
2.2.1.4 Mold fabrication 21
2.2.1.5 PDMS curing 24
2.2.1.6 Oxygen plasma treatment 24
2.2.2 Flow chamber design 26
2.3 EXPERIMENTAL SETUP 28
2.3.1 Experimental plan 29
2.3.2 System synchronization 33
2.4 IMAGE PROCESSING 34
2.5 DATA ANALYSIS 38
2.5.1 Velocity profile 38
2.5.1.1 Particle image velocimetry 38
2.5.1.2 Cross-correlation algorithm 40
2.5.1.3 Velocity profile 41
2.5.1.4 Cell deformation profile 41
2.5.2 Post data processing 41
3.0 RESULTS 43
3.1 PRESSURE CONDITION 43
3.2 FLOW STATUS 44
3.2.1 A few definitions 44

3.2.2 Inside channel 46
3.2.2.1 Velocity distribution across y direction 46
3.2.2.2 Shear stress across y direction 49
3.2.2.3 Wall shear stress 52
3.2.3 At Inlet 52
3.3 CELL DEFORMATION 57
3.3.1 Cell deformation history 57
3.3.2 Cell deformation with changing of flow rate 58
3.3.3 Cell deformation at inlet 60
3.3.4 Cell deformation orientation 61
4.0 DISCUSSION 64
4.1 TWO PHASE FLOW 64
4.2 INLET FLOW 67
4.3 CELL DEFORMATION 72
4.3.1 Deformation at inlet 72
4.3.2 Deformation at outlet 72
4.4 EFFECT OF FLOW RATE 74
5.0 CONCLUSION 78
6.0 FUTURE WORK 79
APPENDIX A 80
APPENDIX B 82
BIBLIOGRAPHY 84

LIST OF TABLES

Table 1 Symbol definition in equation 1-6 19

Table 2 Theoretical value for micro channels..... 20

Table 3 Experimental plan 32

Table 4 Cell deformation data..... 60

Table 5 Cell deformation in four areas 61

LIST OF FIGURES

Fig. 1 Micro-fluidics system, a: syringe pump, b: syringe, c: PVC tubing, d: flow chamber and micro channel, e: reservoir, f: inverted microscope 13

Fig. 2 Channel and chamber assembly 14

Fig. 3 Micro channel coordinate system 15

Fig. 4 Theoretical velocity curve in a micro channel with a rectangular cross section, channel width=150μm, depth=150μm, a: 3D velocity curve, b: bluntness of the curve, solid lines indicate 5^{th} order polynomial regression, dash lines indicate quadratic regression, the difference of solid line and dash line in each flow rate indicates the bluntness 18

Fig. 5 Channel pattern on mask 21

Fig. 6 Micro channel fabrication, a: PDMS pouring, b: micro channels after plasma treatment . 26

Fig. 7 Flow chamber on microscope stage 27

Fig. 8 Experimental set up, 1: plastic syringe, 2: flow chamber and channel, 3: inverted microscope, 4: pulse generator, 5: stroboscope, 6: computer and frame grabber, 7: camera, 8: pressure transducer, 9: multimeter, 10: dial indicator, 11: voltage controller 28

Fig. 9 Experimental strategy 31

Fig. 10 Timing sequence for the experiment 34

Fig. 11 Histogram of original image 35

Fig. 12 Original image 36

Fig. 13 Enhanced image 37

Fig. 14 Histogram of enhanced image 38

Fig. 15 a typical velocity profile on x-y plane 39

Fig. 16 Normalized pressure/flow rate in channel with 150μm width 43

Fig. 17 Mean velocity across y dimension, a: low viscosity sample, solid lines indicate 5th order polynomial regression, dash lines indicate quadratic regression b: high viscosity sample, in channel with 150μm width, solid lines indicate quadratic regression, channel walls are at y=-75μm and y=75μm 48

Fig. 18 Shear rate as increasing flow rate, a: low viscosity sample, b: high viscosity sample, in a channel with 150μm width, channel walls are at y=-75μm and y=75μm, solid lines indicate linear regression 50

Fig. 19 Shear rate comparison between two samples, in a channel with 150μm width, channel walls are at y=-75μm and y=75μm, solid lines indicate linear regression 51

Fig. 20 Wall shear stress, in channel with 150μm width, solid lines indicate linear regression .. 52

Fig. 21 Inlet velocity distribution in x direction, a: distribution, b: the location which velocity distribution is taken from, in channel with 150μm width, the solid lines on Vx(wall) and Vy(wall) indicate 5th order polynomial regression, the solid line on Vx(centerline) indicate linear regression 54

Fig. 22 Inlet velocity distribution in y direction, a: V_x distribution, b: V_y distribution c: the location which velocity distribution is taken from, in channel with 150μm width, the solid lines indicate 5th order polynomial regression, channel walls at y=-75μm and y=75μm.....56

Fig. 23 Cell deformation on x direction, flow rate=0.05ml/min, inlet: x=0, outlet: x=2mm 58

Fig. 24 Cell deformation on x direction as flow rate changes, inlet: x=0, outlet: x=2mm 59

Fig. 25 Cell deformation at inlet 61

Fig. 26 Deformation and velocity direction, a: deformation direction at inlet, b: deformation direction inside channel, c: velocity direction at inlet, d: deformation direction inside channel 63

Fig. 27 Effect of viscosity on velocity profile in micro channel 66

Fig. 28 Effect of viscosity on cell elongation in micro channel 66

Fig. 29 CFD results of inlet flow conditions, flow rate=0.5ml/min, viscosity=30cp, channel width=150μm, (a): extensional stress w/o z component, (b); shear stress w/o z component, (c): extensional stress w/ z component, (d): shear stress w/ z component, (e): extensional stress and shear stress w/ z component, ... 71

Fig. 30 shear stress and velocity at outlet, flow rate=0.5ml/min, viscosity=2cp, channel width=150μm 73

Fig. 31 Cell deformation inside and outside the channel 75

Fig. 32 Relationship of stress and cell elongation, shear stress and extensional stress are calculated from CFD results 76

ACKNOWLEDGEMENT

First of all, I would like to thank my advisor Dr. James Antaki. He gave me a lot of help in the past 2 years. With his guidance, I learned how to finish a research project from developing the research question to writing manuscript, from experiment design to data analysis. When I had problems in my research, he always led me back to the right way. Although I tried to fix the problem by myself, without his suggestion I do not think I could enjoy the joy of success to solve problem by myself. I am really very grateful to his patience and instruction in my MS research in the past years.

Secondly, I want to express my gratitude to Dr. Zhongjun Wu. I used to work in his lab before I switched to current lab. Dr. Wu is an intelligent and diligent researcher. From him, I learned how to carry out the research as well as how to choose the research tools for the research project. He is also the first one who led me to the research field in device-induced blood damage. I appreciate his help and his teaching in the past.

And, I need to thank Dr. Marina Kameneva, who is one of my MS defense committee members. In the past 2 years, I often go to her lab and learn how to use this, how to used that. She is always very kind and full of knowledge. She is the huge source for me in my research projects.

Last but not least, I would like to thank my lab colleagues, who provided me generous help in the last weeks during prepare MS defense. Without them, I could not make it at last for my MS thesis defense. I want to thank all of them for their help. And I also want to thank department of Bioengineering, who provided me the great opportunity to finish my MS thesis defense.

1.0 INTRODUCTION

1.1 BLOOD AND BLOOD DAMAGE

1.1.1 Blood and blood rheology

Blood is a suspension of formed cellular elements in an aqueous solution called plasma [1]. Plasma occupies 55-60% of total blood volume. The main content of plasma is water, which is about 90% by weight. Plasma also contains of 7% plasma protein, 1% inorganic substances and 1% organic substances. The cellular elements occupy the remaining 40-45% of blood volume. There are three kinds of cellular contents, erythrocytes, or red blood cells (RBCs); leukocytes, or white blood cells (WBCs); and platelets. Red blood cells are the most numerous cells, which account for 95%of cellular contents by volume. They conduct the important role of delivering oxygen to the tissue and removing waste from it. Though white blood cells and platelets only contain 5% by volume, they have important roles in immunity and hematostasis, respectively.

1.1.1.1 Macroscopic RBC rheology

Blood rheology has been studied for many years. In a bulk flow, blood shows a non-Newtonian behavior in a low shear rate (<100 s^{-1}), with a decreasing viscosity as shear rate increases [2].

The blood converts to show a Newtonian behavior as the shear rate exceeds 100 s^{-1}. In a near zero shear rate, Cokelet et al. [3] and Merrill et al. [4] showed a finite yield stress, which made blood behave like an elastic solid. Cokelet et al. also showed that the experimental data was able to fit into Casson's equation [5] when the hematocrit is below 33%. Chien et al. [6] illustrated the effects of red blood cell aggregation and deformation on the non-Newtonian behavior of blood flow. They showed that red blood cell aggregation is responsible for the viscosity increase at low shear rate. As the shear rate increased, the disaggregation and the cells deformation causes a decrease in viscosity.

1.1.1.2 Microscopic observation of RBC rheology

In microcirculation, since the diameter of a blood vessel is comparable to the diameter of red blood cells, the blood needs to be considered as a two-phase fluid instead of a homogeneous one. Many studies have been performed to investigate the microscopic behavior of blood flow and blood cells under shear stress in glass capillary and isolated vessels. For cell aggregation, Reinke et al. reported a formation of a cell free plasma layer near the tube wall due to the cell aggregation in a vertically oriented small tube [7]and cell sedimentation on the bottom of the tube when it was horizontally oriented [8].Bishop et al. reported the same situation happen in vivo [9]. Chien et al. observed the cell behavior in shear disaggregation [10]. They concluded that cells separated from each other by rolling rather than sliding.

For cell deformation, Fischer et al. illustrated the cell deformation from biconcave shape to ellipsoid under an increasing shear rate up to 500 s^{-1} using a cone and plate viscometer [11].

They also observed that the orientation of elongation was parallel to the flow direction. They believed there was a membrane rotation, which they described as tank tread, during deformation. Sutera et al. also observed the ellipsoid deformation using a concentric cylinder viscometer [12]. They reported that the cell began to lose the biconcave shape at about 500 dynes/cm^2 and became an ellipsoid when the shear stress exceeded 1500 dynes/cm^2. The cell would be elongated more with continuous increasing of shear stress, with more pointed tips on its two ends. They also reported that the cell would recover to its original shape one minute after the termination of shear stress loading. Those observations illustrated the fluid drop-like deformations of red blood cells in the flow media. The cells can be deformed without changing the surface area and volume under low shear stress conditions.

However, most of the previous microscopic studies are conducted in low shear stress conditions or high-uniform shear stress conditions. None of them are related to the characteristic conditions which red blood cell encounter in cardiovascular devices.

1.1.2 Blood cell damage

Blood cell damage, also called blood trauma, means the pathological changes of cellular elements in blood, including morphologic changes, shortened life span, biochemical functional alterations and complete rupture. Red blood cells can be mechanically destructed due to extremely high shear stress and release hemoglobin. This is defined as “hemolysis”. Platelets can also be stimulated by stress. The platelet aggregation results in thrombosis. Our research stressed on the mechanical damage of red blood cells.

1.1.2.1 Previous studies for RBCs damage

Over the last forty years, many investigations have been performed on flow induced blood trauma. Many of them were conducted to study the shear induced hemolysis in well defined flow conditions. Conventional shear devices, such as cone-and-plate viscometers, concentric cylinder viscometers and capillary tubes, were applied to provide such flow conditions [13] [14] [15]. Blood suspensions were subjected to shear stress for prescribed times and plasma free hemoglobin (fHb) concentration was measured as an index for hemolysis. Those studies showed that there were two primary factors on shear induced hemolysis: shear stress amplitude and loading time. The threshold of shear stress for long exposure times, which is from seconds to minutes, was reported by numerous investigators [14] [16]. Those experiments could not be conducted for a short exposure time on the order of micro seconds. A few investigators also designed novel experimental methods to find the hemolysis status under short exposure times [17]. However, the threshold values in those studies are inconsistent and being debated and revised [18].

These historical studies have provided a general guideline for red blood cell hemolysis. However, the precise mechanisms of blood damage and flow behavior under high shear stress and low exposure time conditions remain unclear.

1.2 DEVICE INDUCED BLOOD DAMAGE

1.2.1 Cardiovascular devices

Cardiovascular disease (CVD) is the No. 1 killer in United States. Over 2,600 people die from CVD every single day. The high mortality of heart diseases urged the development of cardiovascular devices, which could be substituted for part or whole function of the impaired organ. Since 1950s', cardiovascular devices have been developed rapidly. As far as today, prosthetic heart valves replacement has been proved to be a successful treatment to heart valve diseases. Ventricular assist devices (VAD) of varied designing principles have been used either as a temporary bridge for keeping patient alive until later transplantation or as a recovery method for postcardiotomy [19]. Cardiovascular bypass and oxygenator have been used as a standard during the operation through out the world [20]. As a whole, cardiovascular devices are commonly used as a clinical treatment for end stage cardiovascular diseases and improving the survival rate and life qualities for many patients.

1.2.2 Hemolysis induced by implantation, clinical reports

Though enormous amount of research has been done to improve the design and performances of cardiovascular devices over the last two decades, it is still impossible to mimic an exact physiological environment for the blood contacting those devices. The non physiological condition induced by implantation of cardiovascular devices within circulation system acts as a source for multiple complications such as hemolysis and thrombosis. Several clinical researchers have reported the hemolysis complication associated with the implantation of artificial organs in the past two years. Burda et al reported the extracorporeal membrane oxygenation (ECMO)

related hemolysis[21]. Okumiya et al investigated the hemolysis caused by the replacement of cardiac valve prostheses [22]. Allman et al reported an uncommon hemolytic anemia case after the implantation of heart valves [23].

1.2.3 Sublethal blood damage

In addition to hemolysis, cardiovascular devices may also cause sublethal mechanical damage to red blood cells, which cannot be measured through plasma free hemoglobin concentration. Compared to hemolysis studies, very few papers address sublethal blood damage. Artificial organs are found to decrease the deformability of red blood cells [24]. Red blood cells with a low deformability may be prevented from going through the microvessels and may be removed from circulation by spleen. Mechanical stresses have also been reported to change the blood rheology and shorten the life span of RBCs [25].

1.2.4 Previous attempts on design and optimization

Compared to the historical blood damage studies, which were conducted in well defined flow conditions, the flow status in cardiovasular devices is much more complex. A number of in vitro and in vivo studies have been conducted on realistic cardiovascular devices for getting deep knowledge of the characteristic flow pattern, stress-strain conditions, and the blood damage index under specific device working status, for the purpose of optimizing the design to decrease complication rate.

For prosthetic heart valves, researcher stressed on valve closure behavior and pressure-flow conditions. Rebound [26] and squeeze flow [27] phenomena have been found. The regurgitant back flow has been reported to contribute significantly to overall hemolysis in heart valve [28]. In the more complex case of ventricular assistant pump, more criteria need to be considered and a medium needs to be made between the reduction of hemolysis and the adequency of pump working efficiency. Factors such as rotary speed, geometry design, materials choice and surface quality were precisely studied [29] [30] [31] [32]. Flow visualization has been used to directly illustrate the flow conditions around pumps [33]. There are also hemolytic studies being conducted in other implantable devices. For example, Umezu et al. tested the hemolysis level in stentic connectors of different geometries[34]. Sharp et al. reported the hemolysis status in needles and catheters [35].

Most recently, research began to combine numerical simulation and experimental results to seek the correlations between blood stress conditions and damage. Mathematical models for the relationship of stress and hemolysis were established based on experimental data[36] [37]. Computational Fluid Dynamics (CFD) provided a way to estimate and optimize the complicated fluid dynamic situation in multiple cardiovascular devices [38] [39] and predict hemolysis status [40] [41] [42].

The fluid dynamic studies showed that cardiovascular devices induced a non-physiological shear stress, which is much higher than normal, and a quite dynamic flow condition to blood through them. The shear stress distribution is not a uniform one. The highest and most damaging shear stresses are often located in specific regions, which have been referred to as “hot-spots” [43] [44]

[45]. Sharp edges, steps, narrow gaps are the usual "hot-spots" in cardiovascular devices. For instance, in the *StreamLiner* ventricular assist device, an axial blood pump developed by our group [44], the maximum shear stresses are localized in the blade tip region and the leading edge of the stator blades. To achieve the highest pump hydraulic efficiency, blood needs to be moved through a blade tip gap about 50μm wide. The "hot-spots" are regions most likely to cause hemolysis, though only a few individual blood cells in the pump will be subjected to the highest shear stress. The contacting time for the blood through those regions is also very short, which is on the order of micro seconds.

The main contribution of the previous studies is the illustration of the high shear stress, low exposure time conditions faced by surface contacting blood in "hot-spots". A lot of effort was put into optimizing the design of those regions to reduce blood damage. However, most of the designs are conducted in a trial and error fashion, which is a result of the unclear fundamental mechanism of blood deformation and rupture dynamics under the specific environment caused by the implantation of cardiovascular devices. Neither experimental nor CFD modeling research has been conducted in a micro-scale environment with blood considered as a two phase flow. A mathematical model based on a single-continuum, homogenized fluid may lead to the wrong design prediction.

1.3 MOTIVATION

With the increasing use of artificial organs, the blood trauma problem has become an important clinical issue. To overcome blood trauma is a major challenge in the development of implantable cardiovascular devices. However, the fundamental understanding of blood damage associated with characteristic features of cardiovascular devices still remains unclear. Previous fundamental studies are focused on microcirculation, with a low shear stress and a long exposure time. The blood damage studies associated with cardiovascular devices are superficial due to the lack of cell deformation and rupture dynamics under high shear stress, low exposure time conditions. The CFD model was established regardless the two phase nature of blood. All of those issues will slow the development of cardiovascular devices.

The motivation of this project is to resolve the issues risen above. We believe the understanding of device-induced blood damage at a micro-scale level is critical to the long-term success and advancement of cardiovascular device technology.

1.4 AIM OF THESIS

The aim of this project is to find a novel experimental method to 1.understand the dynamic process of red blood cell deformation under non-uniform high shear stress conditions; 2.study the mechanism underlying device-induced hemolysis; 3.provide mechanistic basis for numerical

prediction of blood damage; 4.provide rigorous engineering principles for designing and improving cardiovascular devices.

2.0 METHODS

2.1 SAMPLE PREPARATION

2.1.1 Low viscosity blood sample

Fresh bovine blood was collected in the animal facility at the McGowan Institute for Regenerative Medicine (MIRM). Blood was centrifuged at 3000 RPM for 10 minutes. After centrifugation, plasma and buffy coat, which contains white blood cells and platelets, were removed. Red blood cells (RBCs) then were washed for three times for further removing other blood components. PBS solution (Sigma-Aldrich Corp., St. Louis, MO, 0.01 M phosphate buffer, 0.0027 M potassium chloride and 0.137 M sodium chloride, pH 7.4 at 25 °C) was used as resuspended media in the first two washes and for the third time, 1% bovine albumin (Sigma-Aldrich Corp., St. Louis, MO) was added in PBS solution to prevent RBCs from sticking together.

After washing, the sample hematocrit was measured by capillary centrifuge (IEC Micro MB, IEC Co., Needham Heights, MA). RBCs were resuspended to a needed hematocrit before experiment by adding specified amount of PBS with 1% albumin solution.

The sample hematocrit and viscosity were measured before each experiment, using capillary centrifuge and glass viscometer (Cannon U-tube, Cannon Instrument Co., State College, PA). Temperature was also recorded. For our experiments, hematocrit is (20±2)% and viscosity is (1.8±0.1)cp at ambient temperature (25°C).

2.1.2 High viscosity blood sample

Dextran 40 (Sigma-Aldrich Corp., St. Louis, MO, MW=37,500) was used for making high viscosity RBC suspension. Several preliminary trials had been done to determine the molecular weight (MW) and the concentration of the dextran for experimental using, which is needed to simulate the sample. Low MW dextran was preferred to reduce the possibility of coagulation. The concentration of dextran solution used in the experiment was 30%, with 6g dextran being added to 20g 0.9% sodium chloride solution (Baxter International Inc., Deerfield, IL). The solution was stirred until the dextran was solved completely.

The blood sample was washed using the procedure described in 1.1. Hematocrit was measured after washing. Dextran solution was added to resuspend RBCs to achieve hematocrit of (5±0.2)%. Viscosity was also measured. The resulting viscosity was (30±2)cp.

2.2 MICRO-FLUID SYSTEM

The micro-fluidics system (fig.1) includes a 10ml plastic syringe which was put on a syringe pump (KDS100, KD Scientific Inc., Holliston, MA), a transparent flow chamber with

poly(dimethylsiloxane) (PDMS) micro channel underneath, a reservoir and PVC tubing. A piece of PDMS micro channel was adhered to the bottom of a custom chamber using silicon glue. The channel side faced the bottom and was sealed with a glass slide (fig.2). In the experiment, blood was driven by syringe pump at desired flow rates and forced through micro channel.

The PDMS channel is the crucial component of micro fluid system. The cross section of channel is rectangular to give a good optical access. The edge of channel is smooth and the inlet and outlet have a radius of 15um.

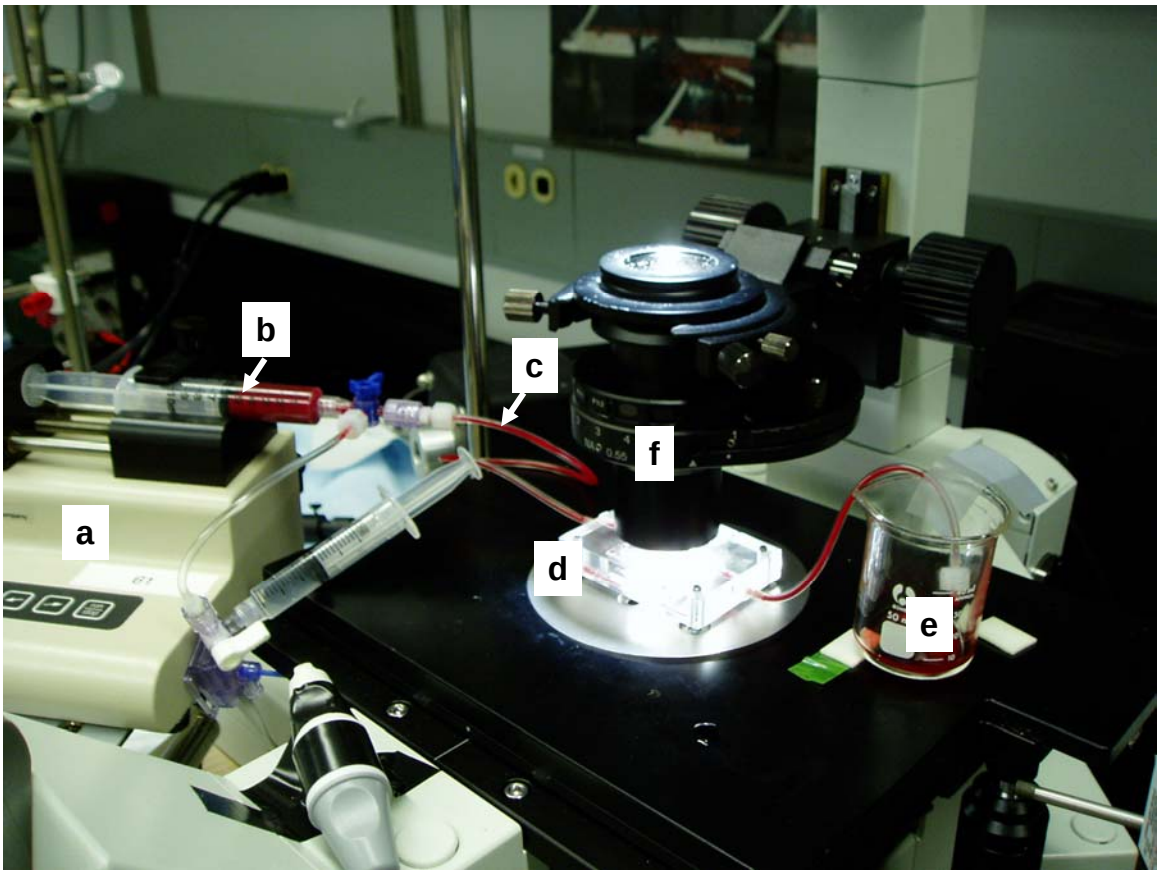

Fig. 1 Micro-fluidics system, a: syringe pump, b: syringe, c: PVC tubing, d: flow chamber and micro channel, e: reservoir, f: inverted microscope

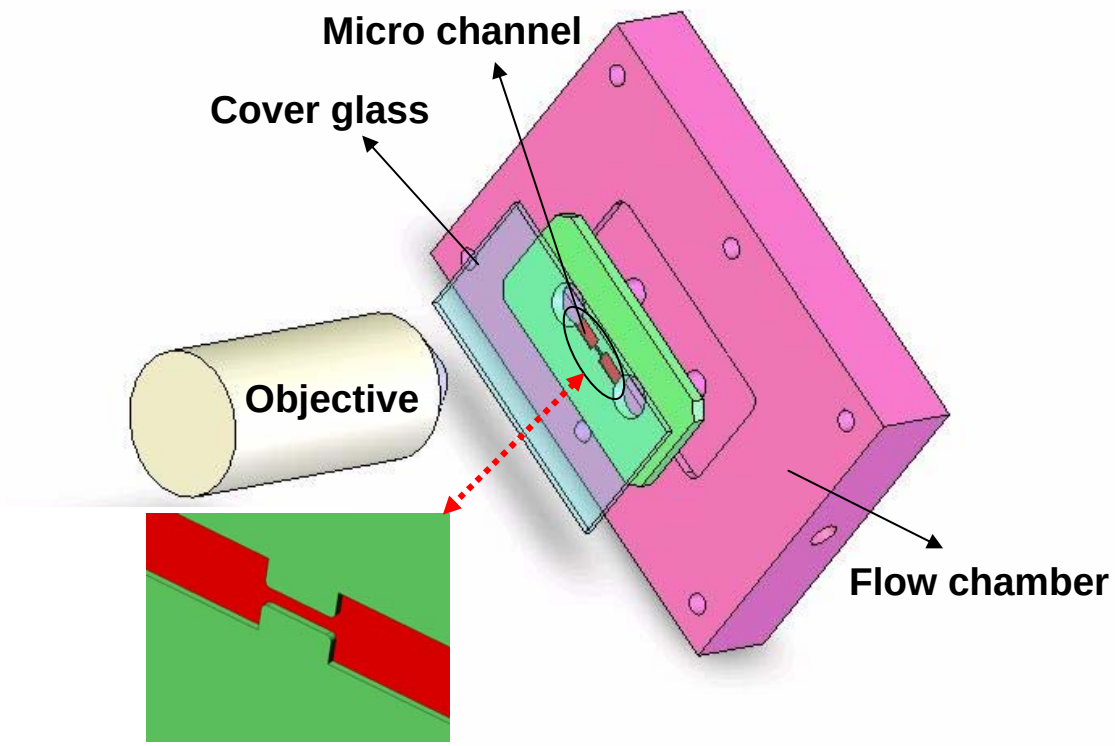

Fig. 2 Channel and chamber assembly

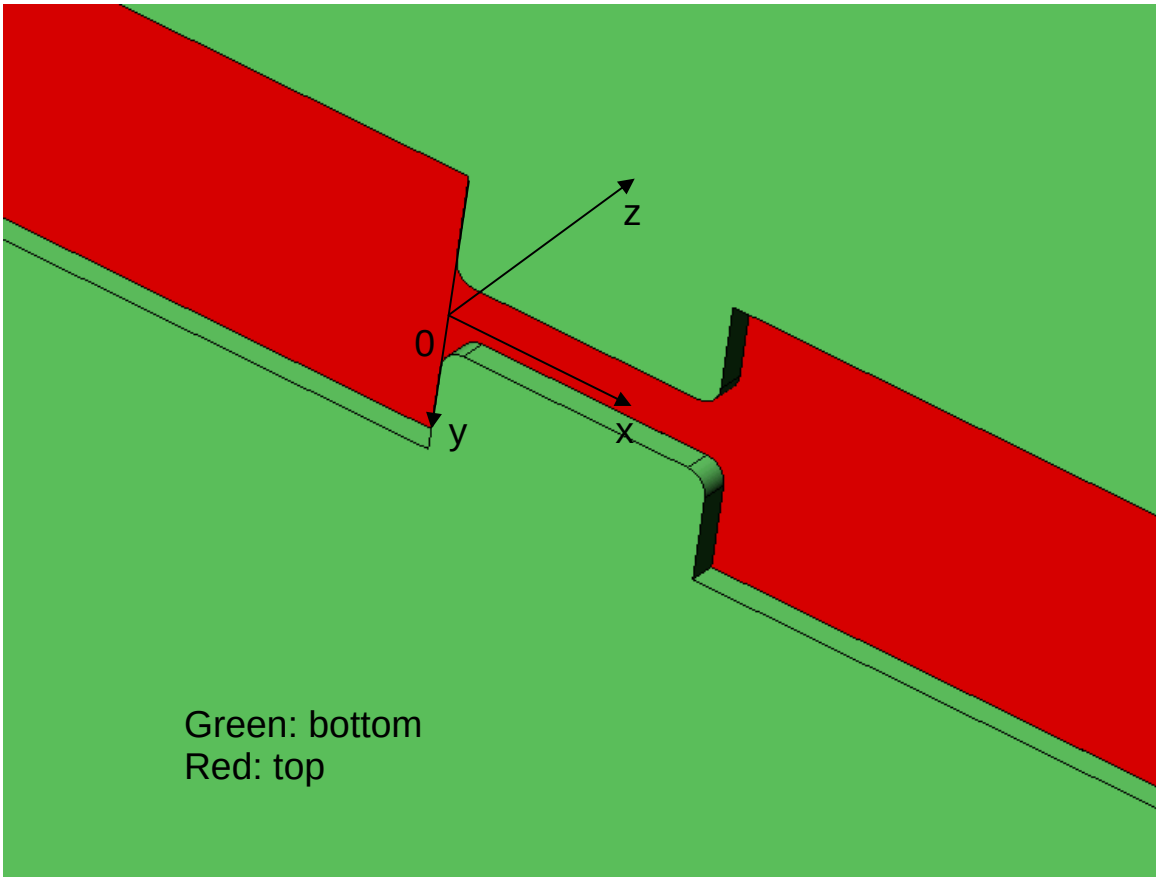

Fig. 3 Micro channel coordinate system

2.2.1 Micro channel design and fabrication

2.2.1.1 Coordinate system

A right-handed Cartesian coordinate system was used to define the micro channel dimensions (fig.3). The x coordinate is parallel to blood flow. The y and z coordinates are aligned to the channel width and depth, respectively. The origin of coordinate is at the intersection of centerline and the line across channel inlet (x=0, y=0) on the bottom plane of the channel (z=0). The x

coordinate increases in the downstream direction. The z coordinate increases as the plane moving from bottom to top.

2.2.1.2 Channel dimension design

The solution for fully developed flow through a duct with rectangular cross section [46] was used as a theoretical guideline for designing channel dimensions, in order to maintain a high shear stress and a short exposure time. Blood was assumed as an incompressible Newtonian fluid to simplify the problem.

$$u(y,z)=\frac{16a^2}{\mu\pi^3}\left(-\frac{d\hat{p}}{dx}\right)\sum_{i=1,3,5,\ldots}^{\infty}(-1)^{(i-1)/2}\left[1-\frac{\cosh(i\pi z/2a)}{\cosh(i\pi b/2a)}\right]\times\frac{\cos(i\pi y/2a)}{i^3} \qquad (1)$$

$$Q=\frac{4ba^3}{3\mu}\left(-\frac{d\hat{p}}{dx}\right)\left[1-\frac{192a}{\pi^5 b}\sum_{i=1,3,5,\ldots}^{\infty}\frac{\tanh(i\pi b/2a)}{i^5}\right] \qquad (2)$$

$(-a\le y\le a,-b\le z\le b)$

The terms in equation1 are defined in table1.

The 3-D velocity profile is shown in figure 4a. At specified x-y plane, the velocity curve is a near parabolic. The cross section geometry causes a small bluntness as shown in figure 4b.

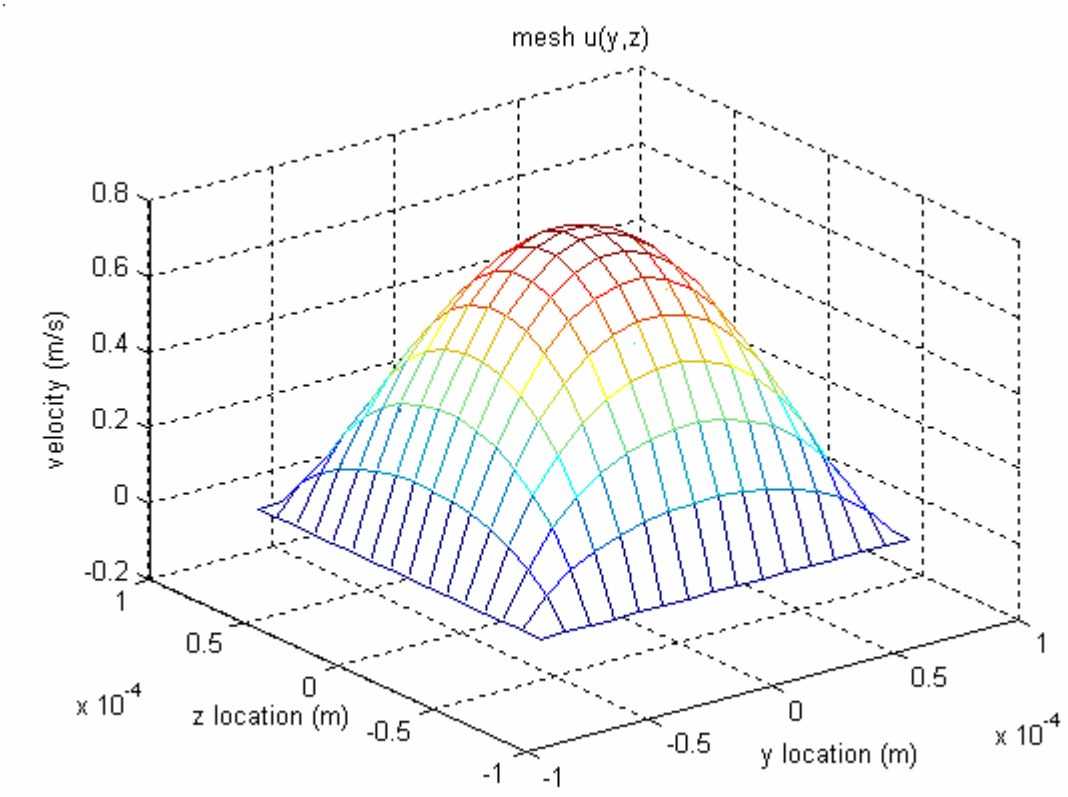
mesh u(y,z)
velocity (m/s)
0.8
0.6
0.4
0.2
0
-0.2
1
0.5
0
-0.5
-1
x 10^-4
z location (m)
-1
-0.5
0
0.5
1
x 10^-4
y location (m)

(a)

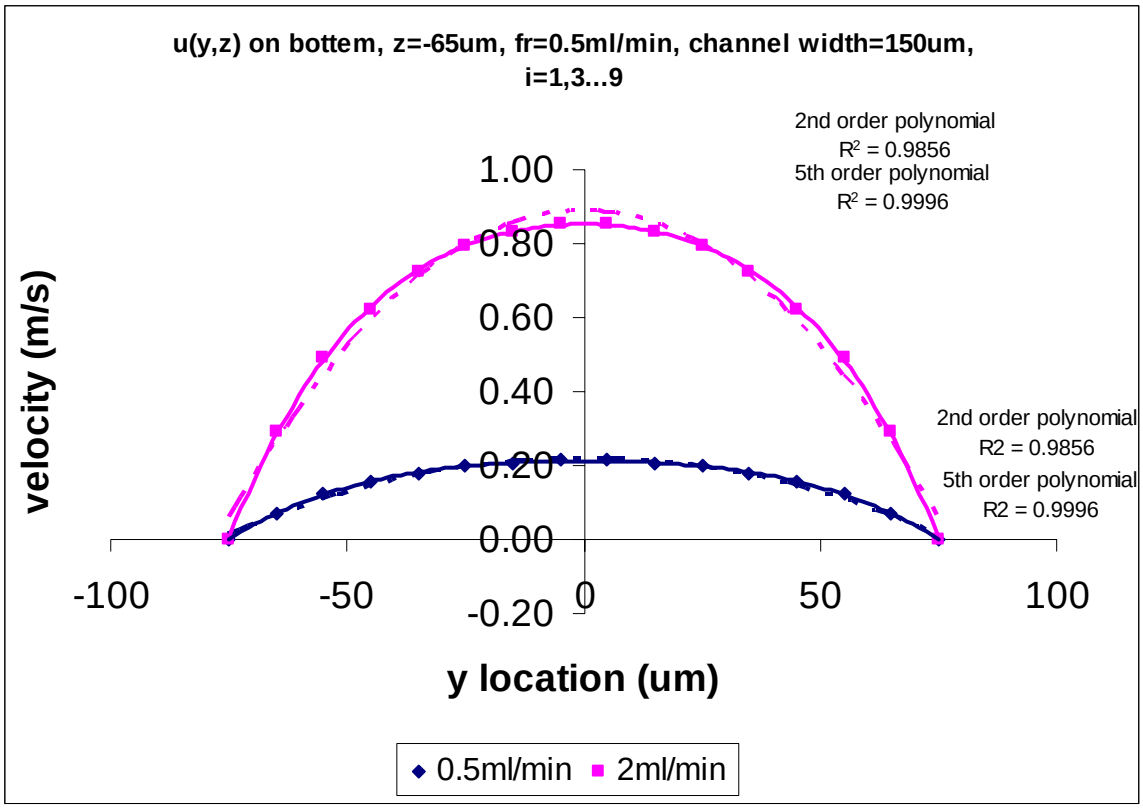

(b)

Fig. 4 Theoretical velocity curve in a micro channel with a rectangular cross section, channel width=150μm, depth=150μm, a: 3D velocity curve, b: bluntness of the curve, solid lines indicate 5th order polynomial regression, dash lines indicate quadratic regression, the difference of solid line and dash line in each flow rate indicates the bluntness

Hydraulic diameter of cross section was introduced to compute Reynolds number of flow in non-circular duct,

$$D_h = \frac{4 \times cross\,area}{wetted\ perimeter} \qquad (3)$$

The equation for calculating Reynolds number is

$$\mathrm{Re}_{d_h} = \frac{\rho \bar{u} D_h}{\mu} \tag{4}$$

The terms in equation6 are defined in table 1.

Table 1 Symbol definition in equation 1-6

Symbol	Definition
a	Half of channel width
b	Half of channel depth
u	Velocity
μ	Viscosity
$\hat{p}$	Pressure
Q	Flow rate
D_h	Hydraulic diameter
Re_{D_h}	Reynolds number
ρ	Density
$\bar{u}$	mean velocity

Table2 shows the theoretical value for the two kinds of channels used in our experiment, which have the same length of 2000μm and depth of 150μm, but have different widths of 50μm and 150μm, for both high viscosity flow (30cp) and low viscosity flow (1.75cp). Because the microscope objective was focused on the plane near bottom, the z plane was assumed as 10μm above the bottom. We can see that the blood inside the channel can be undergoing sufficiently high shear stress and short exposure time, both for a high and low viscosity sample. The Reynolds number is low enough for maintaining a laminar flow.

Table 2 Theoretical value for micro channels

$2a = 50\mu m$				
μ (cp)	1.8	1.8	30	30
Q (ml/min)	0.5	0.1	0.5	0.1
Max γ (s^{-1})	20000	4000	20000	4000
Re_{D_h}	0.1	0.02	$6*10^{-3}$	$1*10^{-3}$
t (ms)	2	9	2	9
$2a = 150\mu m$				
μ (cp)	1.75	1.75	30	30
Q (ml/min)	0.5	0.1	0.5	0.1
Max γ (s^{-1})	10000	2000	10000	2000
Re_{D_h}	0.06	0.01	$4*10^{-3}$	$0.7*10^{-3}$
t (ms)	6	30	6	30

2.2.1.3 Mask design

CorelDRAW (CorelDRAW Graphics Suite 12, Corel Corp., Ottawa, ON) was used to draw the computer drafting file of the mask (fig.5). The size of the mask depends on the characteristic size of the mask holder in the photolithography equipment. In this case, it is a 5×5 inch square. The pattern also needs to be inside a circle, which is homocentric with the mask and whose size is as the same as the silicon wafer. The wafer used in this experiment has a diameter of 4 inches.

The computer file was sent to Magna Graphics Inc. (Pittsburgh, PA), a local company, to be printed out on a transparency using a 3400 DPI high resolution commercial printer. In this case, because we choose SU-8 (SU-8 2075, MicroChem Corp., Newton, MA), a negative tone photoresist, the transparency needs to be printed out positively, which means white area on CorelDRAW file should be clear on the transparency.

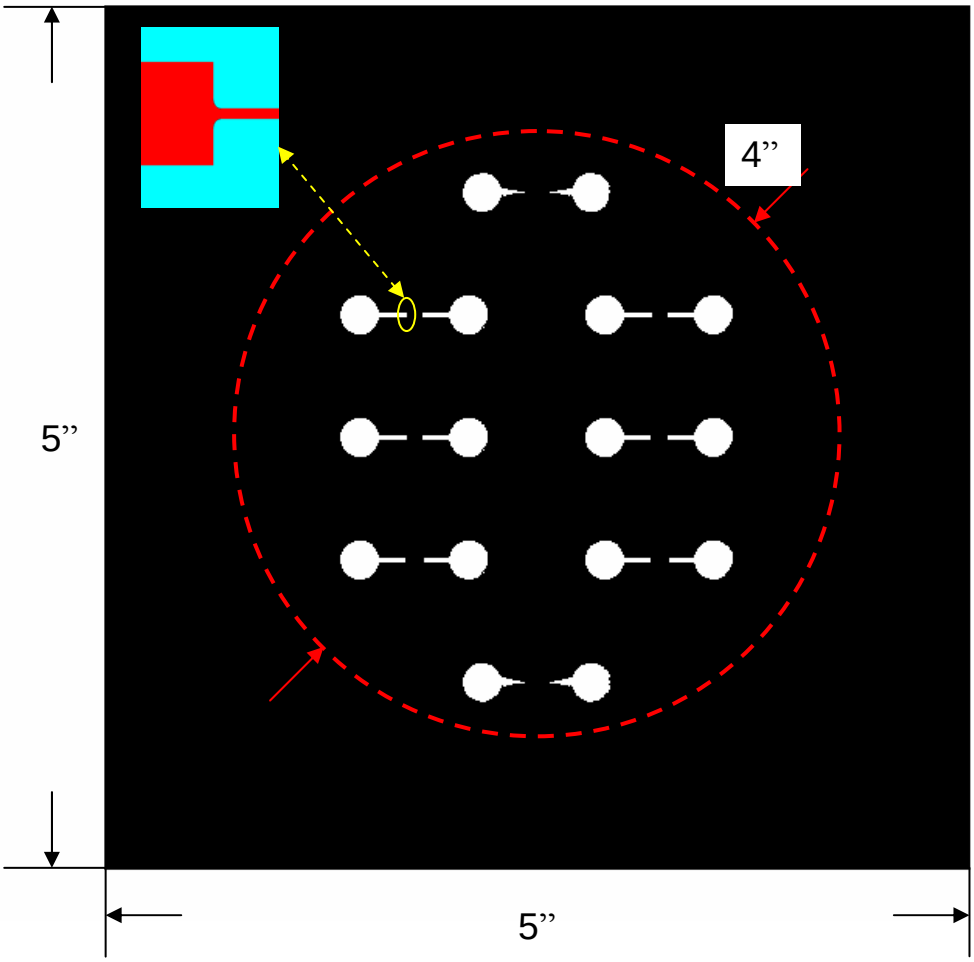

Fig. 5 Channel pattern on mask

2.2.1.4 Mold fabrication

A 5×5 inch square glass plate was used to hold the transparency, which is otherwise too soft to be put on the mask holder in the etching equipment. Margins were justified and the two parts were fixed by placing tape on the edges. Before the transparency and the glass plate were arranged together, both of them were cleaned to remove dust.

Mechanical grade silicon wafers (University Wafer Inc., South Boston, MA) were etched in the clean room of University of Pittsburgh. Since any dust or dirt on the surface of wafer may cause serious problem on SU-8 coating thus causing the whole process to fail, wafer needs to be extremely clean before being put on the spin coater. A process called piranha etch was used to completely clean the wafer. A clean solution was made by mixing sulphuric acid (Mallinckrodt Baker, Inc., Phillipsburg NJ) and hydrogen peroxide together by a ratio of 3:1 by volume. The wafer was washed in the mixture for five minutes and rinsed by deionized (DI) water for ten minutes. The DI water on the surface was blown off by air duster. Then, the wafer was placed on hot plate for five minutes at a temperature of 200°C.

a) Spin coat

After pretreating, the wafer was put on the spin coater (Karl Suss RC8, Suss MicroTec Inc., Waterbury Center, VT). About 5ml of SU-8 was poured at the center of wafer, using caution to avoid inducing air bubbles. The spin coater was was set to 1600rpm for 30 seconds, after which the SU-8 was distributed evenly and became a thin film on the surface.

b) Soft bake

The SU-8 on the wafer surface was soft baked before exposure to UV light. Initially, the wafer was baked for 5 minutes on the hot plate with a temperature of 65°C. Then, the temperature of the hot plate was increased to 95°C at an increasing rate of 2°C/min. The wafer was continuously baked at 95°C for 40 minutes.

c) Exposure

The mask and the soft baked silicon wafer were placed at proper locations with respect to the UV lamp (Karl Suss MA6, Suss MicroTec Inc., Waterbury Center, VT). The UV light was turned on and the wafer was exposed for 30 seconds.

d) Post expose bake

After being exposed, the wafer underwent a post expose bake on the hot place for 1 minute at 65°C and for 15 minutes at 95°C.

e) Develop

About 20ml SU-8 developer (MicroChem Corp., Newton, MA) was poured into a glass tray and placed in the developer for ten minutes. The SU-8 in non-exposed areas was washed out during this process, while the SU-8 in exposed areas remained on the surface and became hard. After being developed, the wafer was washed in Isopropyl Alcohol to remove SU-8 developer. After washing, the wafer surface should be bright and clean. If there is a white film on the surface, it means some SU-8 has not been fully developed and still remained on the wafer surface. In that case, the wafer needs to be developed again in a new SU-8 developer. After being washed in IPA solution, the wafer was washed by DI water to get rid of IPA on surface.

f) Hard bake

Finally, the mold was put on the hot plate and baked for 30 minutes at 200°C. The purpose of this process is to harden the pattern on the mold.

2.2.1.5 PDMS curing

PDMS (Sylgard 184, Dow Corning Corp., Midland, MI) was made by mixing silicon elastomer base and curing agent in a 10:1 ratio by weight. The mixture was then centrifuged for about 20 seconds to remove air bubbles due to the reaction during mixing. Silicon mold was placed in the center of a container. PDMS was poured over the mold in the center slowly, to avoid inducing more bubbles (fig.6a).

The container was placed in a vacuum oven for further removal of bubbles. The vacuum pump was turned on until the pressure inside decreased to -23 in. Hg. The low pressure remained steady for 2 minutes. During this period, the air bubbles were seen swelling and floating to the surface of PDMS. After 2 minutes, the pressure was increased quickly to pop as many bubbles as possible. The process was repeated several times until the majority of small bubbles had gone. After removing from the container, large air bubbles that were still in the PDMS were popped manually with a small needle. The container was then heated at 60°C for four hours to cure the PDMS. Cured PDMS was removed from container by loosening edges with a scraping tool. This step was done very carefully, avoiding breaking the mold. After the PDMS piece was successfully separated from mold, it was cut to individual channels to fit into the channel shell. Two reservoir holes were punched assuming smooth edges.

2.2.1.6 Oxygen plasma treatment

The channel was sealed with a glass slide by oxygen plasma treatment [47], which was conducted in the laboratory of Dr. Shelley Anna from Department of Chemical Engineering, at

Carnegie Mellon University (CMU). Both glass slide and channel had been completely cleaned with detergent, DI water and acetone before the treatment. Then, they were placed in the plasma cleaner (Harrick PFC-32G, Harrick Scientific Corp., NY) for 1 minute and put together quickly after being taken out (fig.6).

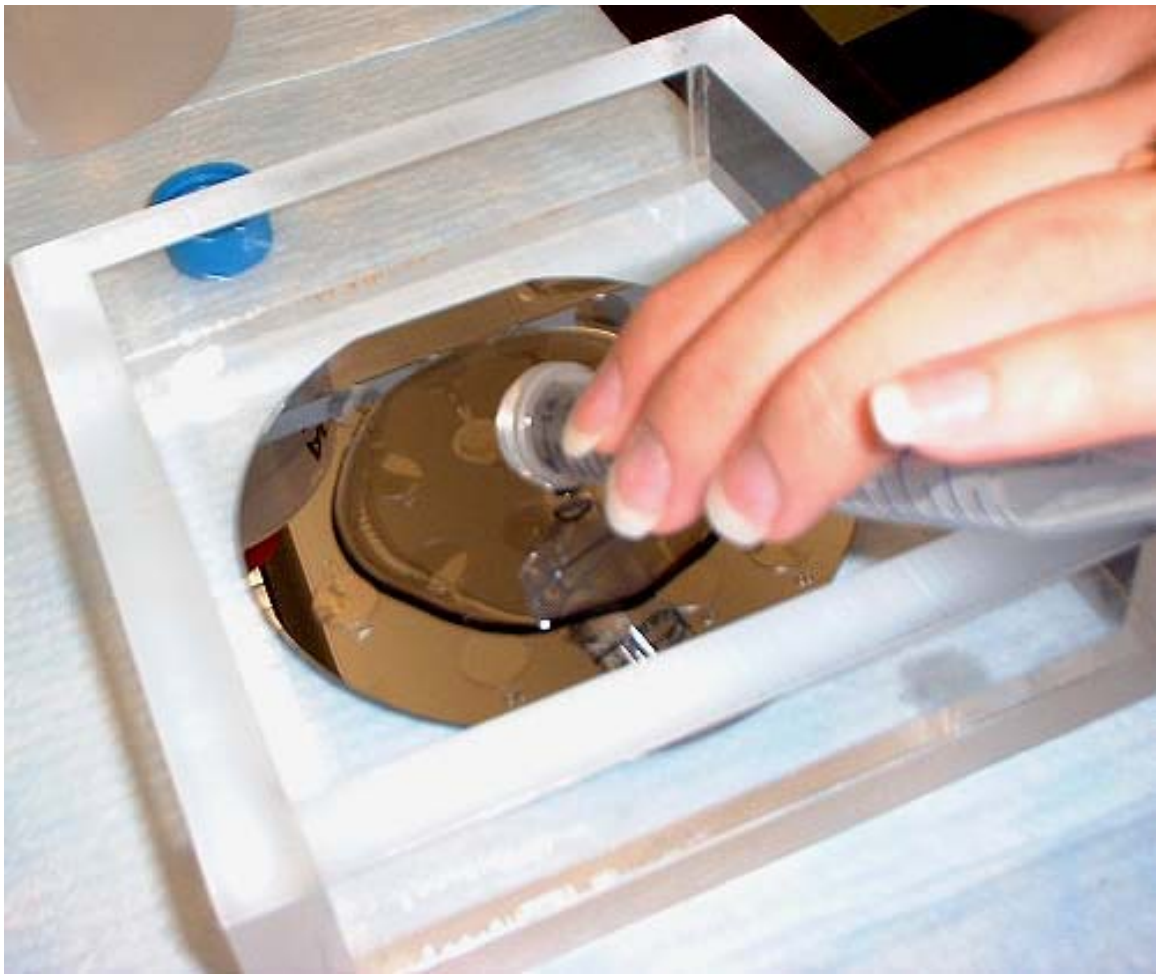

(a)

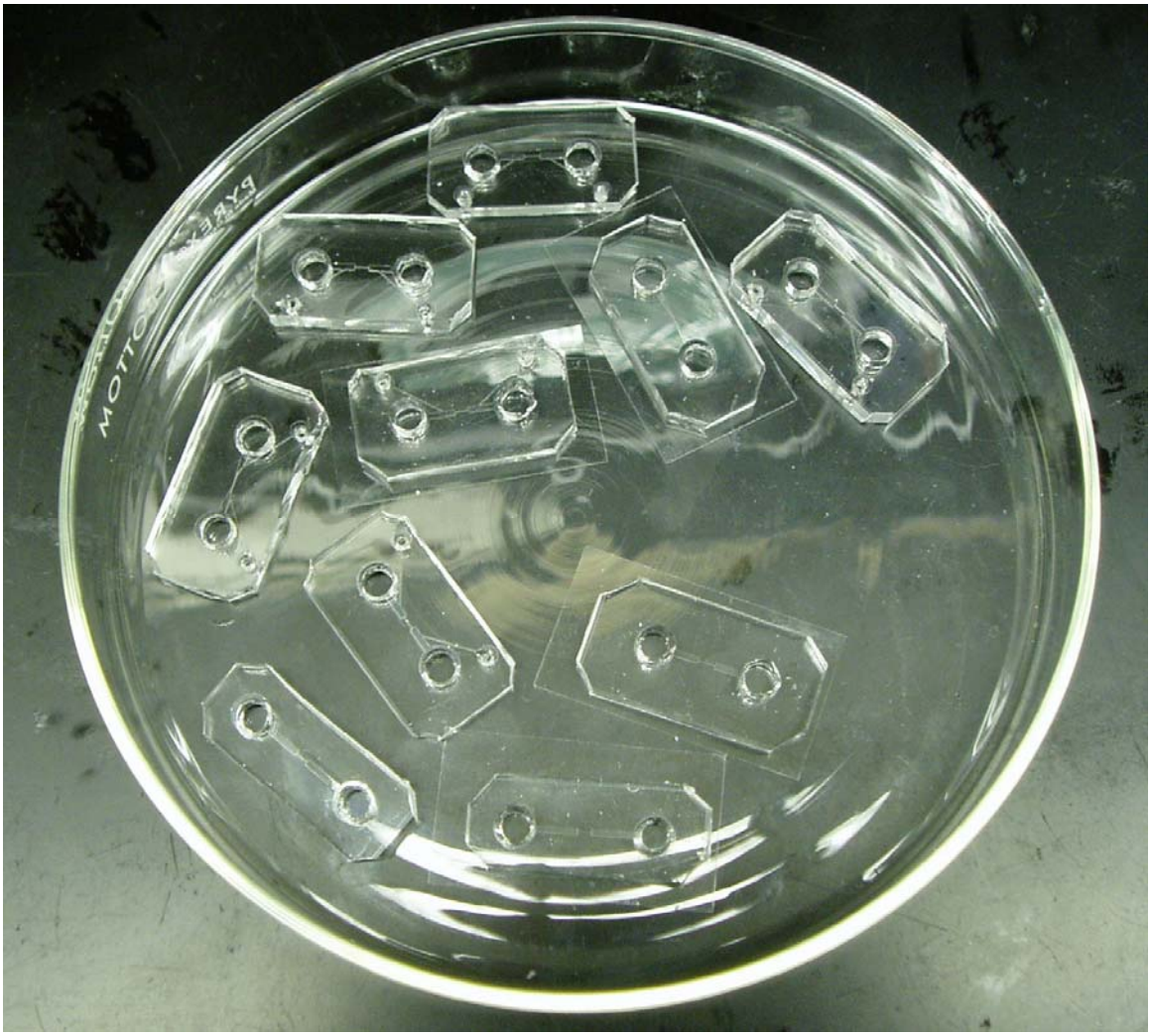

(b)

Fig. 6 Micro channel fabrication, a: PDMS pouring, b: micro channels after plasma treatment

2.2.2 Flow chamber design

A polycarbonate flow chamber (fig.7) was designed to hold the PDMS micro channel and give an easy optical pathway. The back side of PDMS piece was stuck under the chamber by silicon glue. The surfaces of chamber were polished to give a good optical pathway. The flow chamber was fixed on the stainless steel plate, which was specifically designed for the chamber, with four

screws. The plate was fitted to the hole on the microscope stage. The channel through camera can be easily adjusted to be parallel to the image frame by circling the plate. The four screws were helpful in making the whole image field focused. Input and output tubing were connected and sealed with silicon glue.

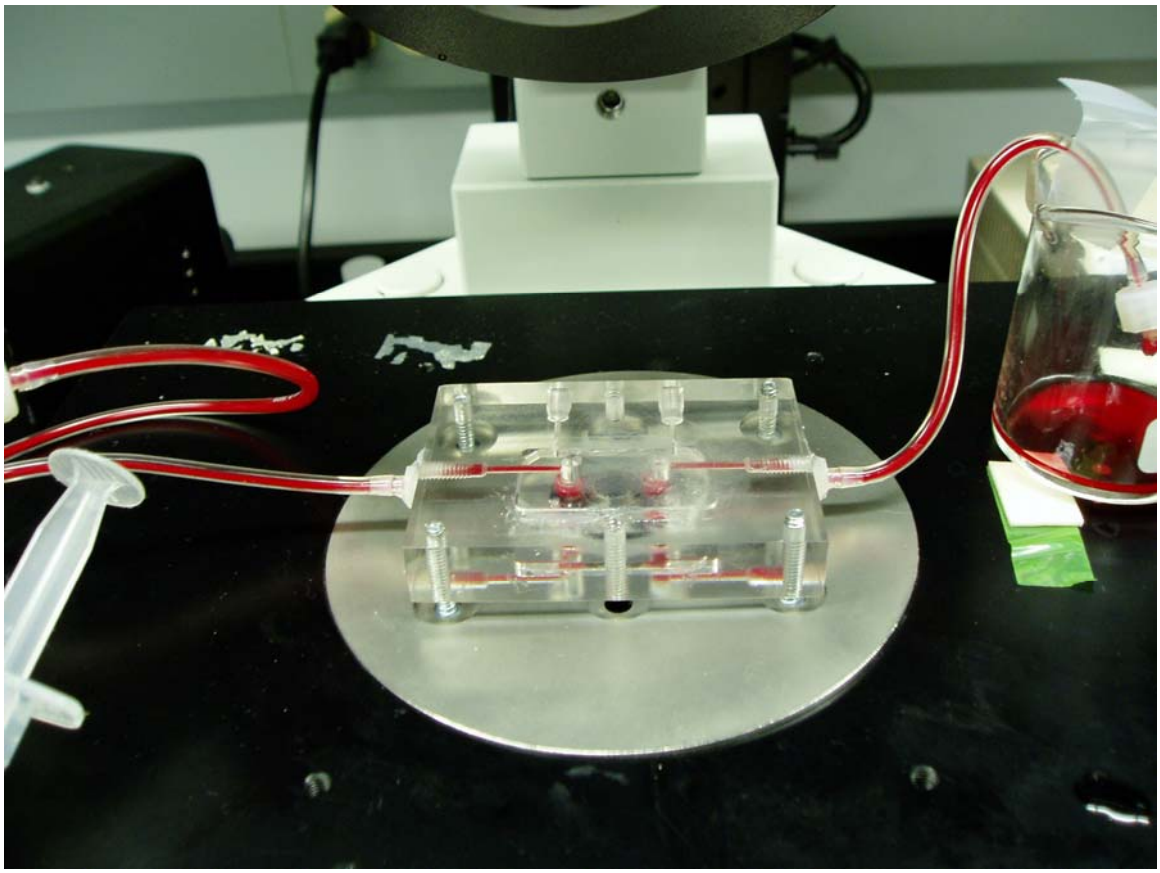

Fig. 7 Flow chamber on microscope stage

2.3 EXPERIMENTAL SETUP

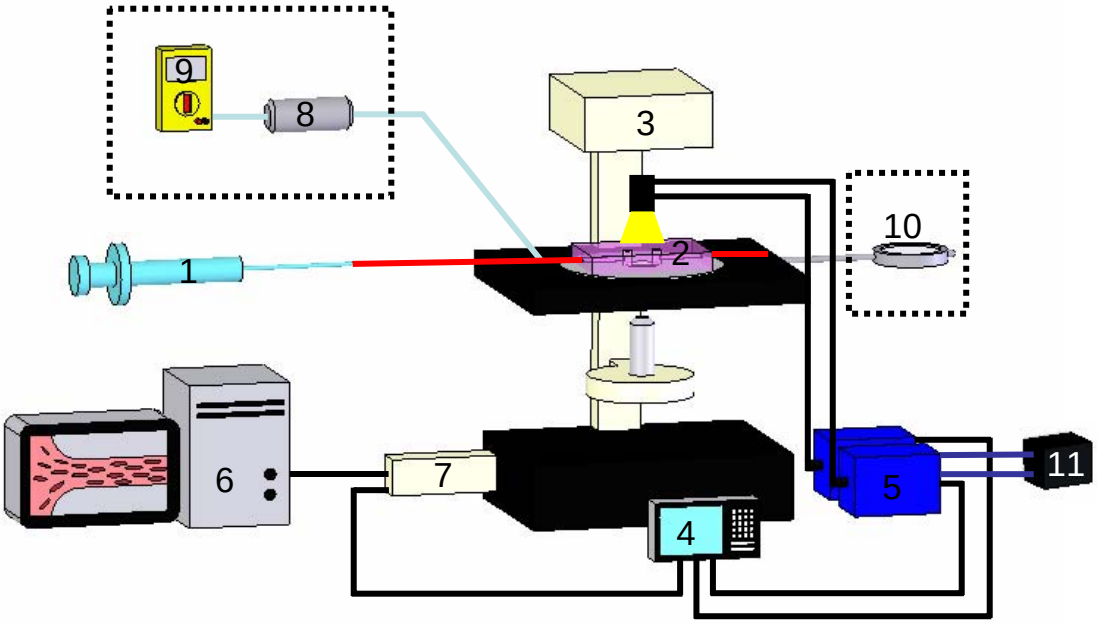

Fig. 8 Experimental set up, 1: plastic syringe, 2: flow chamber and channel, 3: inverted microscope, 4: pulse generator, 5: stroboscope, 6: computer and frame grabber, 7: camera, 8: pressure transducer, 9: multimeter, 10: dial indicator, 11: voltage controller

The overall experimental setup is shown in figure 8. In the experiment, blood was loaded in a 10ml plastic syringe ((1), Becton, Dickinson and Company, Franklin Lakes, NJ), which was driven by a syringe pump. The blood was pushed through the micro channel and collected in a reservoir. The flow chamber (2), with PDMS micro channel underneath, was fixed on the stage of an inverted microscope ((3), Olympus IX70, Olympus, Melville, NY). Both chamber and PDMS piece were transparent to allow sufficient light transmission. A digital camera ((7), Princeton Instruments MicroMax, Roper Scientific Inc., Rochester, NY) was hooked up to the microscope to capture the image from objective to the frame grabber on a computer (6).

Two stroboscopes ((5), X400, PerkinElmer Optoelectronics Inc., Wellesley, MA) were used as illuminators, which were connected in parallel by a two-in-one fiber-optic cable with the output end fixed above the chamber. A voltage controller (11) was connected to both of the stroboscopes in order to make the two output beam intensities approximately equal to each other. Both the stroboscopes and the camera were connected to a pulse generator ((4), BNC500, Berkeley Nucleonics Corp. San Rafael, CA) to be synchronized. A pair of images, with a very short separation time between them, was captured by camera. Each of them was illuminated by one of the two stroboscope beams.

2.3.1 Experimental plan

Figure 9 shows the overall experimental strategy. Low and high viscosity samples were mainly used to obtain velocity profile and cell deformation profile, respectively. A dial indicator (10) was placed on one side of the stage to measure the axial location. The zero point was set as the inlet edge was on the left side of image frame on computer screen. The accuracy of the dial is 0.001 inches, which equal to 25.4μm. After setting the image to a specified location, blood was pushed with different flow rates. In each flow rate, pressure was measured from a port which was close to the tubing-chamber connection by a pressure transducer (8) and 10 pairs of images were acquired.

Both 40× and 100× magnification objectives were used in the experiments. The 40× objective (Olympus UPlanFL, 40×, NA=0.75) was mainly used to capture images for calculating velocity profile, while the 100× (Olympus UPlanFL, 100×, NA=1.30) was used to observe the cell

deformation. In this experiment, because the cover glass was very thin, it was possible to use objective with a relatively short working distance.

Table 3 shows the location and flow rate used in the experiments. For the high viscosity sample at flow rate of 0.05, 0.1 and 2 ml/min, the microscope stage was moved from 2mm before channel inlet to 2 mm after the channel outlet, and images were taken from 30 locations with a distance of 0.008 inches (about 200μm). The protocol allowed us draw a dynamic picture of RBCs from the collector to diffuser.

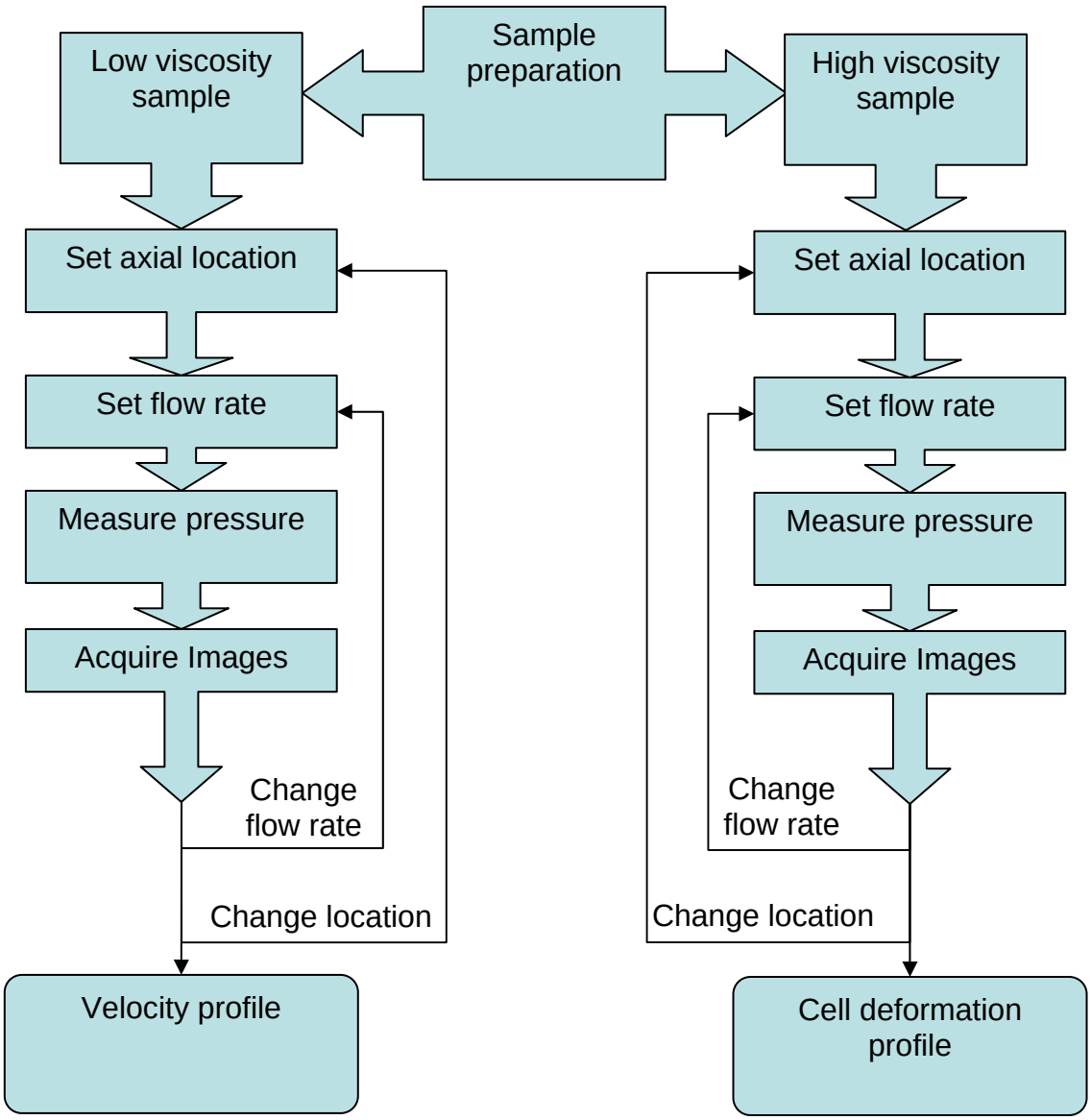

Fig. 9 Experimental strategy

Table 3 Experimental plan

Flow rate (ml/min)	Low viscosity sample		High viscosity sample (30 locations in x direction)				
	Channel inlet	Inside channel	x= -2mm	…	x=1mm (Inside channel)	…	x= 4mm
0.05			10 pairs of image deforma-tion	10 pairs of image each location deforma-tion	10 pairs of image deforma-tion	10 pairs of image each location deforma-tion	10 pairs of image deforma-tion
0.1			10 pairs of image deforma-tion	10 pairs of image each location deforma-tion	10 pairs of image deforma-tion	10 pairs of image each location deforma-tion	10 pairs of image deforma-tion
0.2	10 pairs of image velocity	10 pairs of image velocity	10 pairs of image deforma-tion	10 pairs of image each location deforma-tion	10 pairs of image deforma-tion	10 pairs of image each location deforma-tion	10 pairs of image deforma-tion
0.3					10 pairs of image deforma-tion		
0.4	10 pairs of image velocity	10 pairs of image velocity			10 pairs of image deforma-tion		
0.5					10 pairs of image deforma-tion		
0.6	10 pairs of image velocity	10 pairs of image velocity					
0.8	10 pairs of image velocity	10 pairs of image velocity					
1.0	10 pairs of image velocity	10 pairs of image velocity			10 pairs of image deforma-tion		
2.0					10 pairs of image deforma-tion		

2.3.2 System synchronization

The camera and two stroboscopes needed to be synchronized. A four channels pulse generator was used to generate external trigger signals for stroboscopes and camera. A proper timing sequence was needed according to the characteristic of stroboscopes and camera. The factors affecting the timing sequence, such as the delay time between external signals and illuminator light, the illuminator pulse duration and camera intrinsic timing, were considered to set up the timing sequence.

For the camera, an external signal was used to trigger the first exposure. The exposure time and the separation time between two exposures were set by the WinView software. After the separation time, the second exposure was started. There is no need to generate a trigger signal for the second exposure. Timing sequence for the experiment is illustrated in figure 10. There is a 10μs delay time between trigger signal and strobe light. The light duration is 8-10μs. There is also a 200ns intrinsic time between the increasing edge of camera trigger signal and camera exposure, which is too small to show in the figure.

The exposure time and separation time needed to be properly set according to the experimental conditions. Due to the light output duration of stroboscopes, the separation time could not be shorter than 10μs. The exposure time was set according to the image qualities on the computer screen. The location of the fiber-optic head and the intensity adjustment controller also contributed to the image qualities.

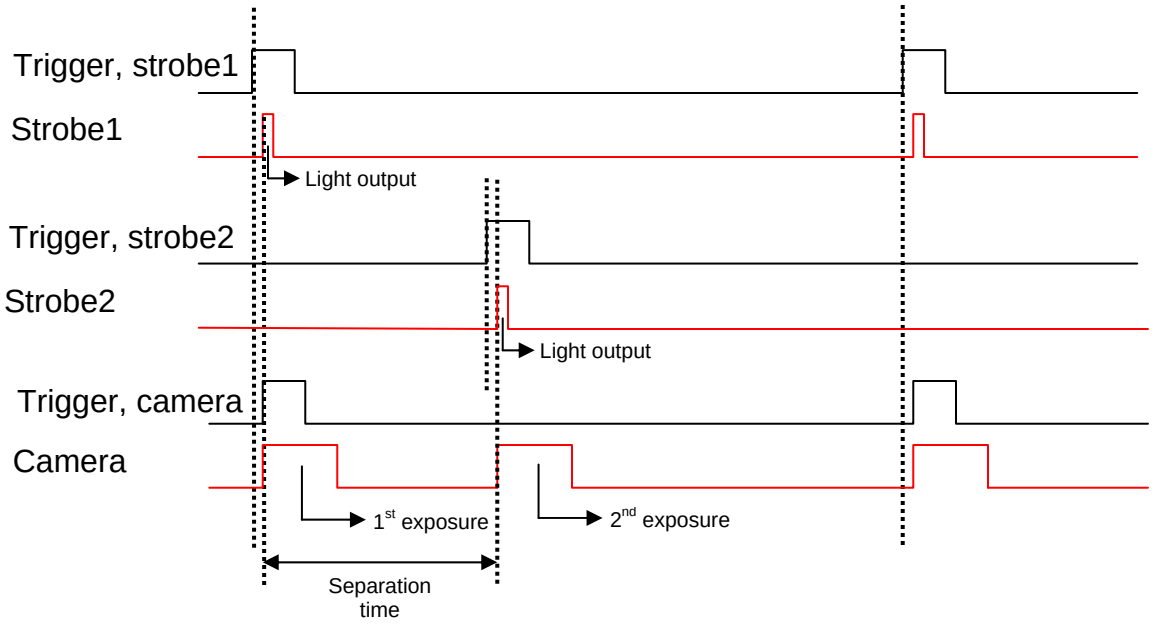

Fig. 10 Timing sequence for the experiment

2.4 IMAGE PROCESSING

Matlab (MathWorks Inc., Natick, MA) Image Processing Tool Box was used to write image processing program ("separation.m" in Appendix). The histogram of a typical original image was shown in figure 11. In this histogram, the pixels concentrated in [40,210] gray level instead of covering the whole extent of gray level. The limit of gray level gradient made the image have a poor contrast between the interested object and background (fig.12). The image was equalized by setting all the non frequency gray level to either zero or 255 and widening other pixel gray level distributions proportionally to their originally ones. That allows the diversity be enlarged so that contrast was improved (fig.13, fig.14).

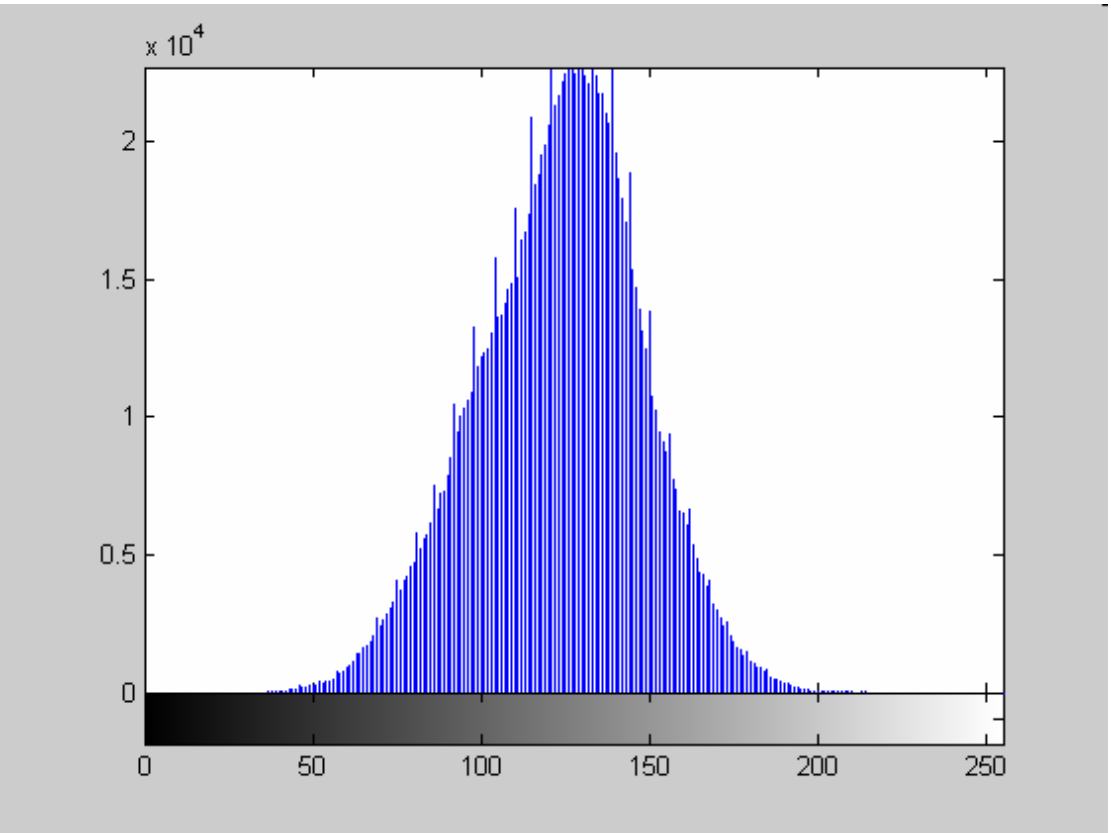

Fig. 11 Histogram of original image

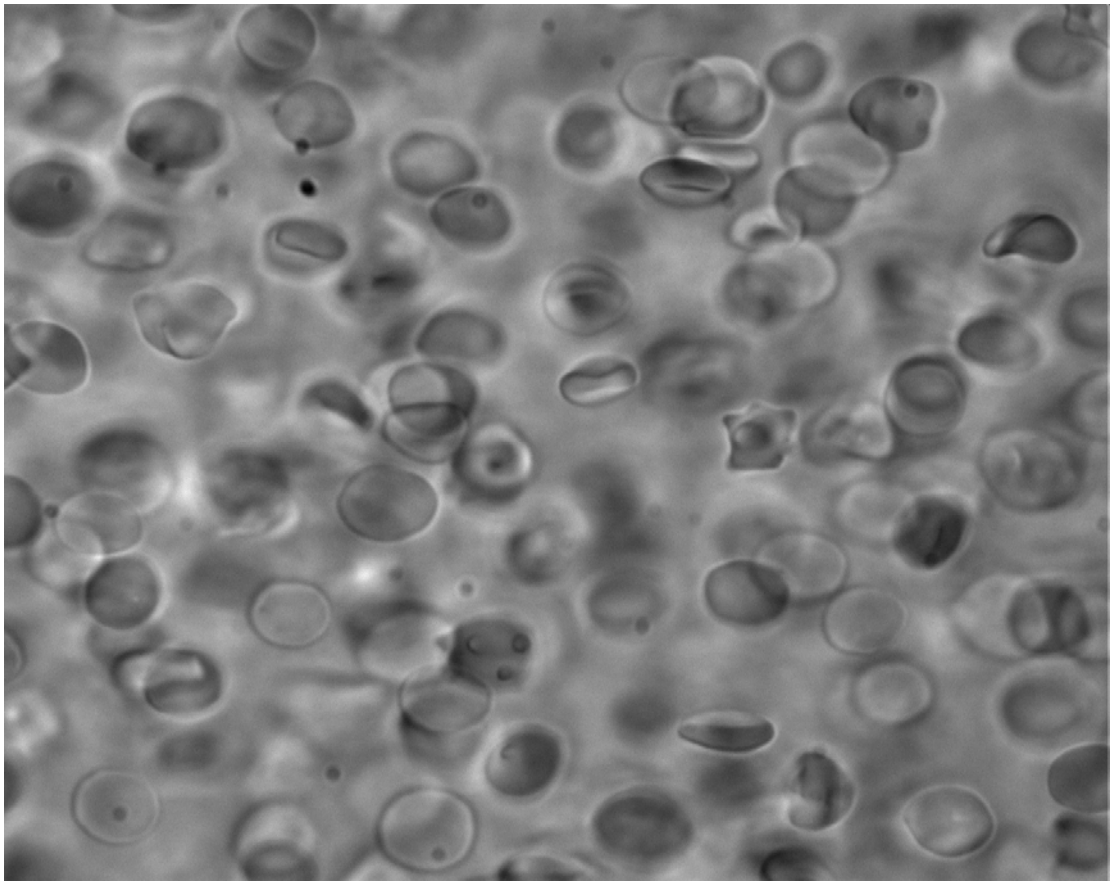

Fig. 12 Original image

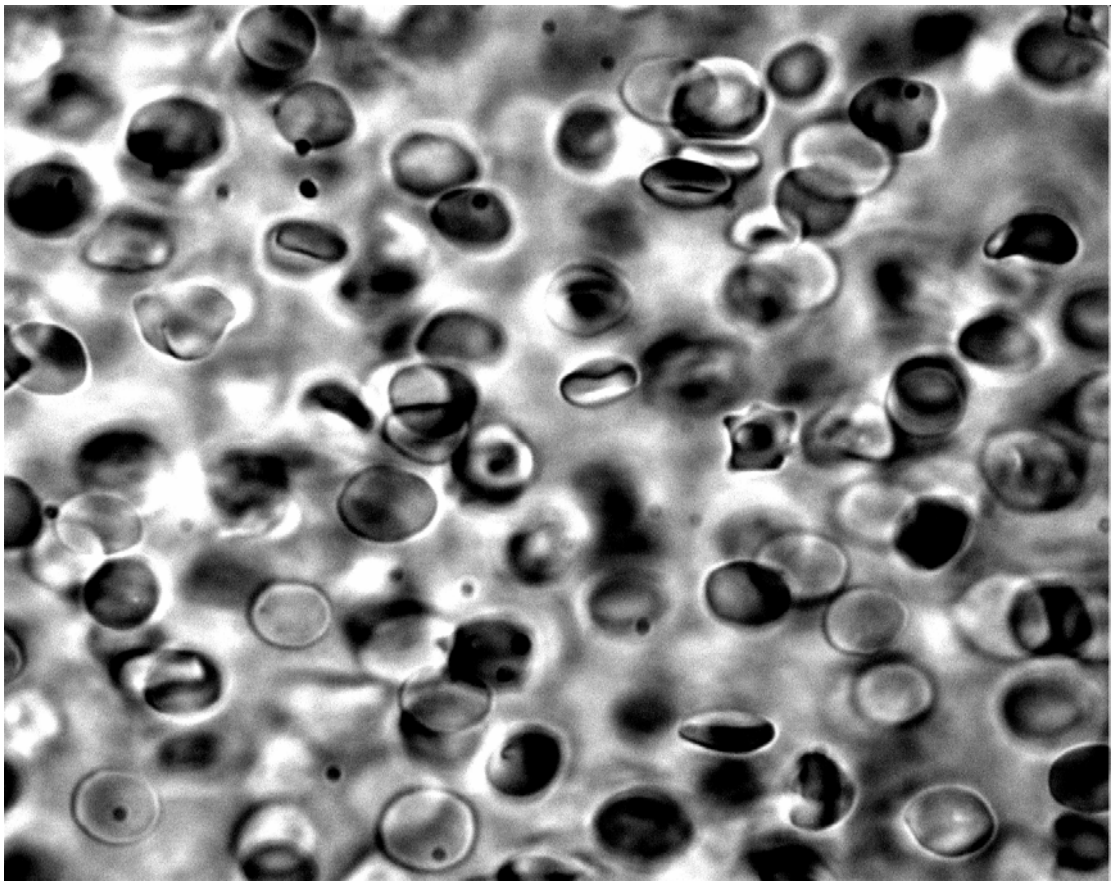

Fig. 13 Enhanced image

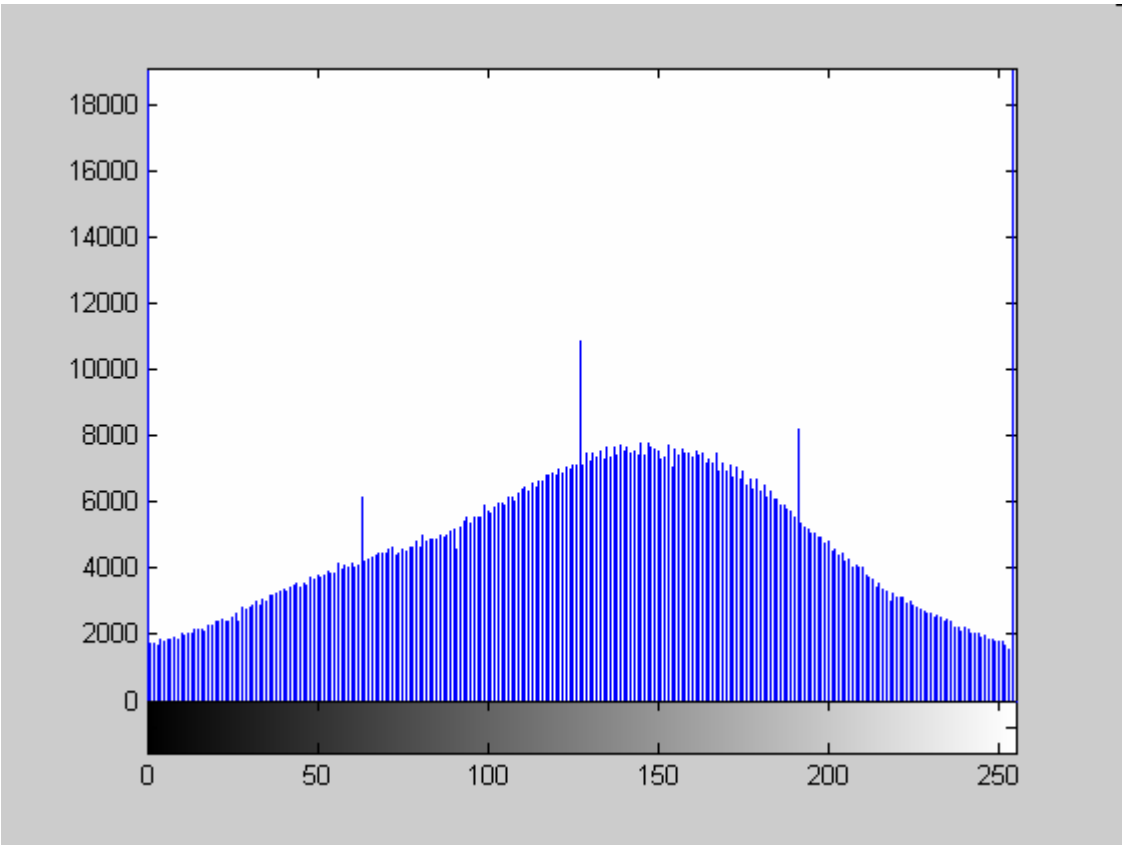

Fig. 14 Histogram of enhanced image

2.5 DATA ANALYSIS

2.5.1 Velocity profile

2.5.1.1 Particle image velocimetry

Particle image velocimetry (PIV) was used to measure the two-component velocity field of blood flow in the x-y plane. In PIV, image was separated to a matrix of subregions named interrogation

windows. The average displacement of tracer particles in each interrogation window was measured. Velocity was calculated using equation7.

$$V = \frac{\Delta x}{M \bullet \Delta t} \qquad (5)$$

Where, Δx is the average displacement of tracer particles, M is the optical system magnification and Δt is the separation time.

In this experiment, red blood cells were regarded as tracer particles, by assuming they were small enough to follow the flow accurately. Images taken with a 40× objective were used to measure velocity profile and were separated to a matrix of 64×64 pixel interrogation windows. Figure 15 is the typical velocity profile extracted from experiment. It shows that this experimental setting is good enough to measure velocity profiles on x-y plane.

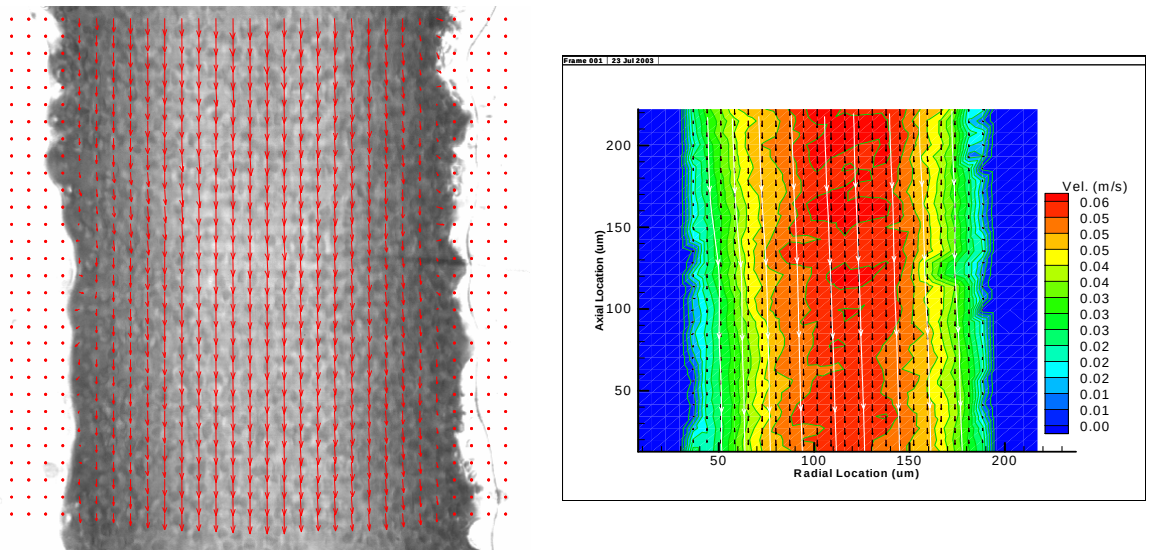

Fig. 15 a typical velocity profile on x-y plane

2.5.1.2 Cross-correlation algorithm

For Particle image velocimetry, it is impossible to track individual particles. The average displacement of tracer particles needed to be calculated statistically. In this experiment, double frame/single exposure images were taken and cross-correlation algorithm was used to calculate the average displacement of tracer particles in each interrogation window. The definition of cross-correlation function for digitally recorded images is:

$$R_{fg}(i,j) = f(i,j) \otimes g(i,j) = \sum_{x=0}^{M}\sum_{y=0}^{N} f(i,j)g(x-i,y-j) \qquad (6)$$

Where, $R_{fg}(i,j)$ is the intensity of the $(i,j)^{\text{th}}$ pixel on resulting cross-correlation image, $f(i,j)$ and $g(i,j)$ are the intensity of the $(i,j)^{\text{th}}$ pixel on the pair of original images. M and N are the x and y dimension of interrogation windows, respectively.

The function is normalized to remove the effect of brightness variation:

$$R_{fg}(i,j) = \frac{\sum_{x=0}^{M}\sum_{y=0}^{N}[f(x,y)-\overline{f}][g(x-i,y-j)-\overline{g}]}{\sigma_f \sigma_g} \qquad (7)$$

Where, $\overline{f}$ and $\overline{g}$ are the average intensity value of the images. σ_f and σ_g are their standard deviations. The normalized $R_{fg}(i,j)$ is varied between -1 and 1.

The cross-correlation function can be considered as the combination of correlation between particle pairs and correlation between different particles, which are called random correlations. The particle-pairs correlation is constant and will generate a peak which is much higher than the

peak generated by random correlations. According to the algorithm, the distance between this peak and the center of the cross-correlation image is the average displacement of tracer particles.

2.5.1.3 Velocity profile

A software, PIVPROC (Glenn Research Center, NASA), was used to process the displacement data using cross-correlation algorithm. This software can generate a .VEC file whose format which can be read by TechPlot.

A 15×19 data matrix was generated, in which each node is denoted as the average displacement of one 64×64 interrogation window. The two-dimension location of each node was also recorded in the data file.

2.5.1.4 Cell deformation profile

Matlab program (AppendixA) was used to measure cell deformation. The two cell length ends were picked up manually, according to the observed cell edge. The two dimension cell elongation data and cell location data were generated through Matlab program.

2.5.2 Post data processing

Data was post processed using Matlab. All data were saved in specified ".txt" files for further using. For cell displacement data generated by PIVPROC, the mean and standard deviation displacement in each interrogation window was created by averaging data from ten images. For

cell displacement inside channels, the data from the same row were further averaged assuming there was no velocity change in x direction. Before averaging the data from the same row, the zero data and those data with angles more than 10° departure from x axis, which were regarded being generated by mistake, were excluded from results(AppendixB). After averaging data, the displacement data was converted to the velocity data by dividing the separation time between images. Shear rate data were generated from velocity data. For cell deformation data, the average cell deformation in one location was generated by averaging all the cell deformations in ten images.

3.0 RESULTS

3.1 PRESSURE CONDITION

The input pressure of both the high viscosity sample and the low viscosity sample was measured and recorded (fig.16). The pressure increased linearly (R^2>0.99) as flow rate increasing in both sample. The slopes were very close to each other (12.3 vs 12.1). These results showed that the experimental conditions were not changed in these two sets of experiments and there was no micro channel expansion due to too much pressure in both experiments.

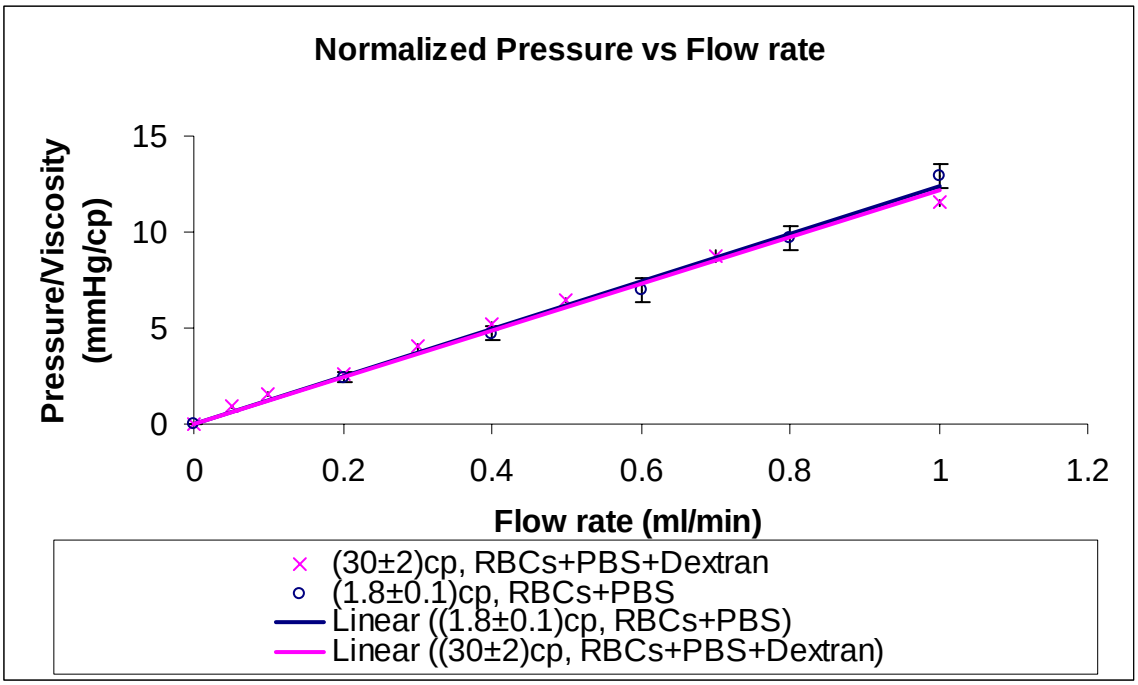

Fig. 16 Normalized pressure/flow rate in channel with 150μm width

3.2 FLOW STATUS

3.2.1 A few definitions

Before analyzing fluid flow conditions, we need to specify the equation and definition to describe the flow field. First of all, we need to make some assumptions for the flow conditions. We assume the sample is an incompressible Newtonian fluid. Also, we assume that we look for a local model when stress depends only on the local gradient of the flow.

We define $\underline{\underline{E}}$ as the strain rate tensor. Then

$$\underline{\underline{E}} = \frac{1}{2}(\nabla \underline{V} + \nabla \underline{V}^T) \tag{8}$$

Where, $\underline{V}$ is the velocity vector [48]. For a 3-D flow

$$\underline{V} = [V_x \quad V_y \quad V_z] \tag{9}$$

$$\underline{\underline{E}} = \frac{1}{2}\left(\begin{bmatrix} \frac{\partial V_x}{\partial x} & \frac{\partial V_x}{\partial y} & \frac{\partial V_x}{\partial z} \\ \frac{\partial V_y}{\partial x} & \frac{\partial V_y}{\partial y} & \frac{\partial V_y}{\partial z} \\ \frac{\partial V_z}{\partial x} & \frac{\partial V_z}{\partial y} & \frac{\partial V_z}{\partial z} \end{bmatrix} + \begin{bmatrix} \frac{\partial V_x}{\partial x} & \frac{\partial V_y}{\partial x} & \frac{\partial V_z}{\partial x} \\ \frac{\partial V_x}{\partial y} & \frac{\partial V_y}{\partial y} & \frac{\partial V_z}{\partial y} \\ \frac{\partial V_x}{\partial z} & \frac{\partial V_y}{\partial z} & \frac{\partial V_z}{\partial z} \end{bmatrix}\right) \tag{10}$$

$$\underline{\underline{E}} = \frac{1}{2}\begin{bmatrix} 2\frac{\partial V_x}{\partial x} & \frac{\partial V_x}{\partial y} + \frac{\partial V_y}{\partial x} & \frac{\partial V_x}{\partial z} + \frac{\partial V_z}{\partial x} \\ \frac{\partial V_y}{\partial x} + \frac{\partial V_x}{\partial y} & 2\frac{\partial V_y}{\partial y} & \frac{\partial V_y}{\partial z} + \frac{\partial V_z}{\partial y} \\ \frac{\partial V_z}{\partial x} + \frac{\partial V_x}{\partial z} & \frac{\partial V_z}{\partial y} + \frac{\partial V_y}{\partial z} & 2\frac{\partial V_z}{\partial z} \end{bmatrix} \tag{11}$$

We define two simple flow models: shear flow and extensional flow. The strain rate is the off diagonal component for shear flow.

The strain rate expression caused by shear flow

$$\underline{\underline{E}}_{shear} = \frac{1}{2}\begin{bmatrix} 0 & \frac{\partial V_x}{\partial y}+\frac{\partial V_y}{\partial x} & \frac{\partial V_x}{\partial z}+\frac{\partial V_z}{\partial x} \\ \frac{\partial V_y}{\partial x}+\frac{\partial V_x}{\partial y} & 0 & \frac{\partial V_y}{\partial z}+\frac{\partial V_z}{\partial y} \\ \frac{\partial V_z}{\partial x}+\frac{\partial V_x}{\partial z} & \frac{\partial V_z}{\partial y}+\frac{\partial V_y}{\partial z} & 0 \end{bmatrix} \tag{12}$$

The strain rate expression caused by extensional flow

$$\underline{\underline{E}}_{ext} = \begin{bmatrix} \frac{\partial V_x}{\partial x} & 0 & 0 \\ 0 & \frac{\partial V_y}{\partial y} & 0 \\ 0 & 0 & \frac{\partial V_z}{\partial z} \end{bmatrix} \tag{13}$$

The magnitude of $\underline{\underline{E}}$ is defined as

$$\left|\underline{\underline{E}}\right| = \sqrt{\frac{1}{2}(\underline{\underline{E}} : \underline{\underline{E}}^T))} \tag{14}$$

$$\left|\underline{\underline{E}}\right| = \sqrt{\frac{1}{2}(E_{11}{}^2 + E_{12}{}^2 + E_{13}{}^2 + E_{21}{}^2 + E_{22}{}^2 + E_{23}{}^2 + E_{31}{}^2 + E_{32}{}^2 + E_{33}{}^2)} \tag{15}$$

[49]

For shear flow,

$$\left|\underline{\underline{E}}\right|_{shear} = \frac{1}{2}\sqrt{(\frac{\partial V_x}{\partial y}+\frac{\partial V_y}{\partial x})^2 + (\frac{\partial V_z}{\partial y}+\frac{\partial V_y}{\partial z})^2 + (\frac{\partial V_x}{\partial z}+\frac{\partial V_z}{\partial x})^2} \tag{16}$$

For extensional flow,

$$\left|\underline{\underline{E}}\right|_{ext} = \sqrt{\frac{1}{2}[(\frac{\partial V_x}{\partial x})^2 + (\frac{\partial V_y}{\partial y})^2 + (\frac{\partial V_z}{\partial z})^2]} \tag{17}$$

For a Newtonian fluid, stress and strain rate have the relationship of $\underline{\underline{\sigma}} = 2\mu\underline{\underline{E}}$. The magnitude of stress can be denoted as

$$\left|\underline{\underline{\sigma}}\right|_{shear} = 2\mu\left|\underline{\underline{E}}\right|_{shear} = \mu\sqrt{(\frac{\partial V_x}{\partial y} + \frac{\partial V_y}{\partial x})^2 + (\frac{\partial V_z}{\partial y} + \frac{\partial V_y}{\partial z})^2 + (\frac{\partial V_x}{\partial z} + \frac{\partial V_z}{\partial x})^2} \tag{18}$$

$$\left|\underline{\underline{\sigma}}\right|_{ext} = \mu\left|\underline{\underline{E}}\right|_{ext} = 2\mu\sqrt{\frac{1}{2}[(\frac{\partial V_x}{\partial x})^2 + (\frac{\partial V_y}{\partial y})^2 + (\frac{\partial V_z}{\partial z})^2]} \tag{19}$$

For a flow inside channel, $V_y = V_z = 0$. $\left|\underline{\underline{\sigma}}\right|_{shear}$ is simplified to

$$\left|\underline{\underline{\sigma}}\right|_{shear} = \mu\left|\underline{\underline{E}}\right|_{shear} = \mu\sqrt{(\frac{\partial V_x}{\partial y})^2 + (\frac{\partial V_x}{\partial z})^2} \tag{20}$$

3.2.2 Inside channel

3.2.2.1 Velocity distribution across y direction

Figure 17 shows the mean velocity along the y direction for low and high viscosity samples in channel with 150μm width. The curve fit well to a parabolic curve (R^2>0.98). The figure also shows the 5th order polynomial regression of the data, which could be accurate to R2=0.999. It shows that the bluntness only has slight effect near wall. We can get the shear rate component $\frac{\partial V_x}{\partial y}$ from velocity profile. To simplify the problem, we assume a parabolic velocity profile, regardless the very small bluntness due to the cross section geometry. The velocity data were

smoothed to the second order polynomial curve when they were used to calculate shear rate $\frac{\partial V_x}{\partial y}$ profile. By this assumption, we can get a linear shear rate profile and it will be easier for the analysis afterwards.

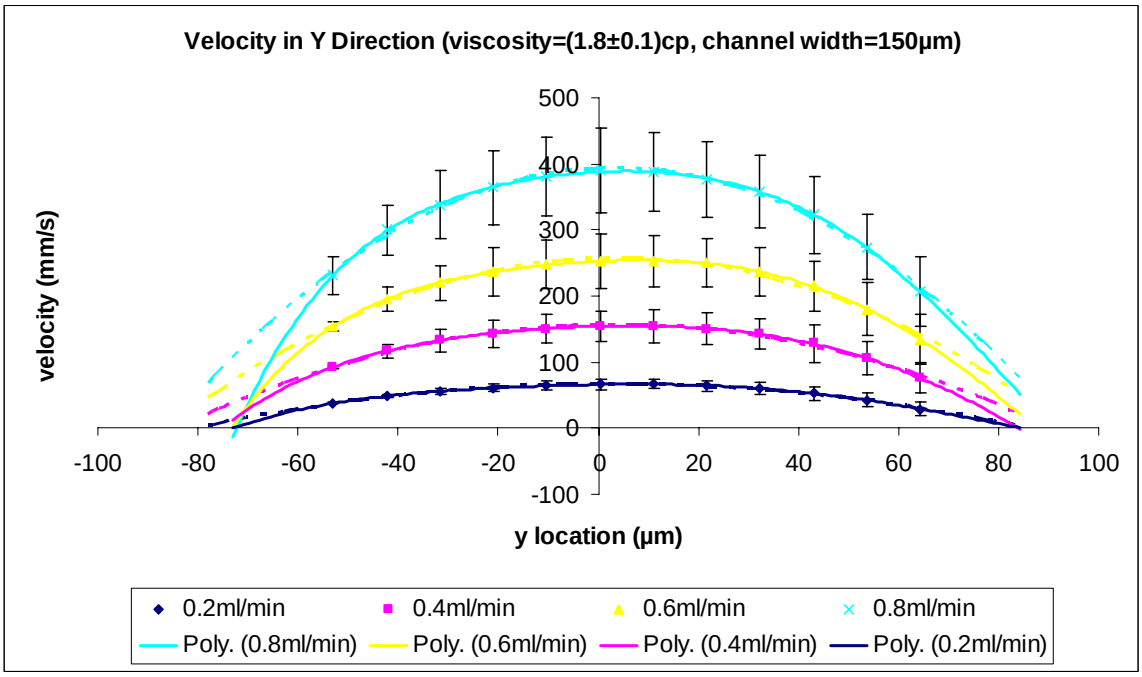

(a)

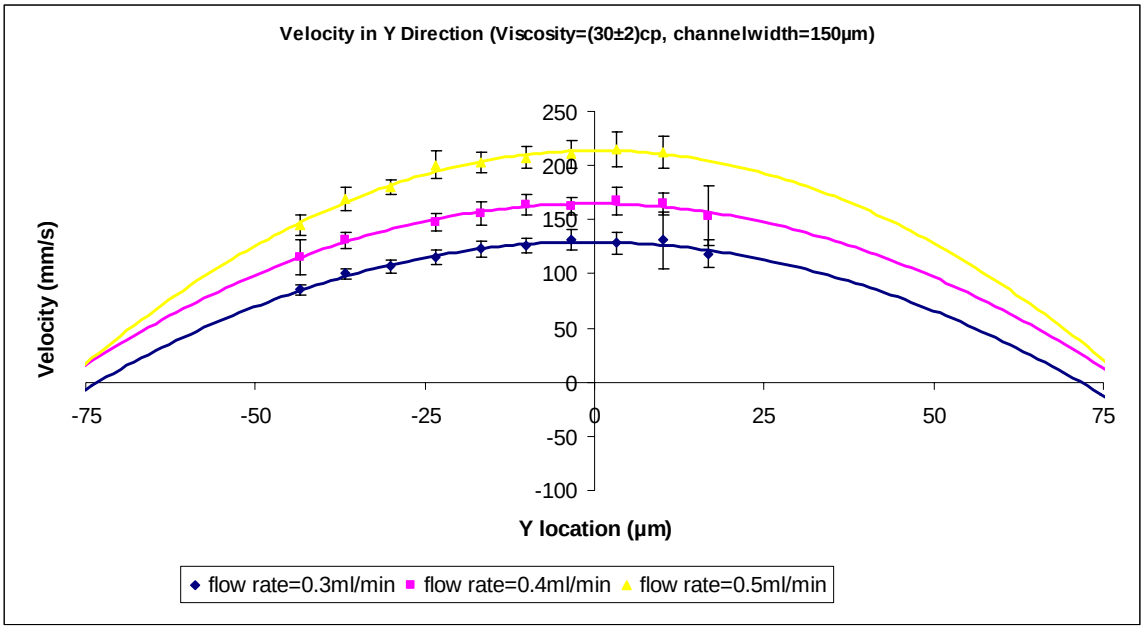

(b)

Fig. 17 Mean velocity across y dimension, a: low viscosity sample, solid lines indicate 5th order polynomial regression, dash lines indicate quadratic regression b: high viscosity sample, in channel with 150µm width, solid lines indicate quadratic regression, channel walls are at y=-75µm and y=75µm

3.2.2.2 Shear stress across y direction

Figure 18 shows the shear rate component $\frac{\partial V_x}{\partial y}$ increase as the flow rate increases for low and high viscosity samples in channel with 150µm width. The shear rate slope increased with increasing flow rate for both sample. The shear rate and shear stress are denoted a direction change instead of the arbitrary values so that it is easy to add a trend.

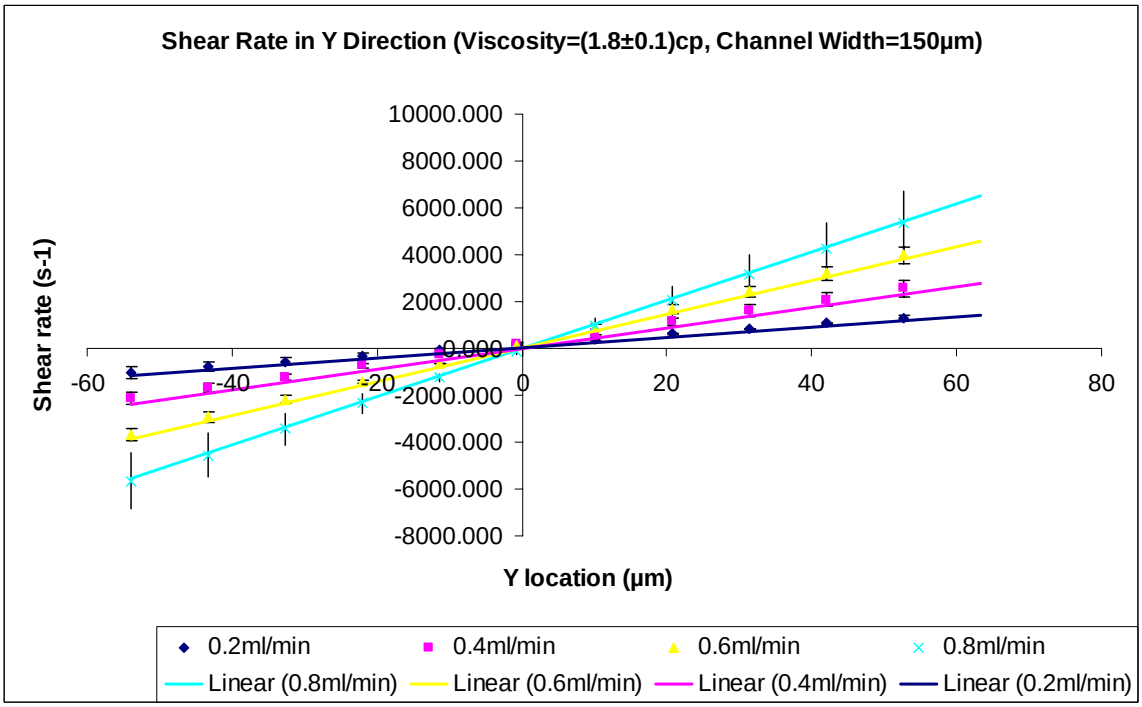

(a)

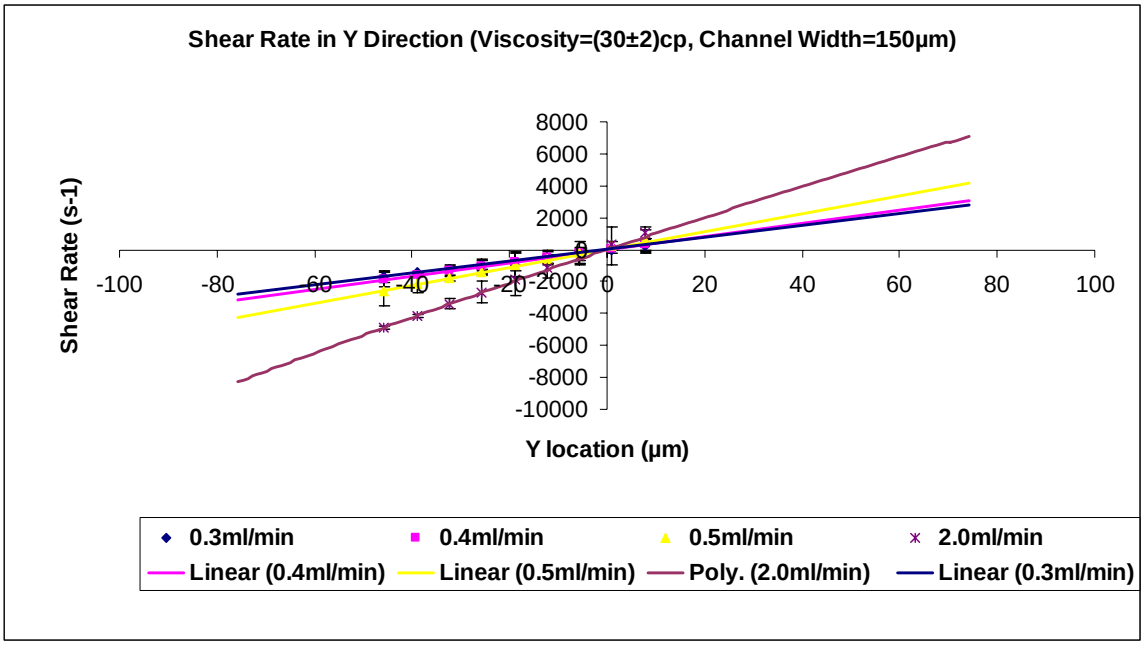

(b)

Fig. 18 Shear rate as increasing flow rate, a: low viscosity sample, b: high viscosity sample, in a channel with 150μm width, channel walls are at y=-75μm and y=75μm, solid lines indicate linear regression

Figure 19 shows the comparison of shear rate distribution in the y direction between the high viscosity sample and the low viscosity sample, in channel with 150µm width. The shear rate is approximately the same.

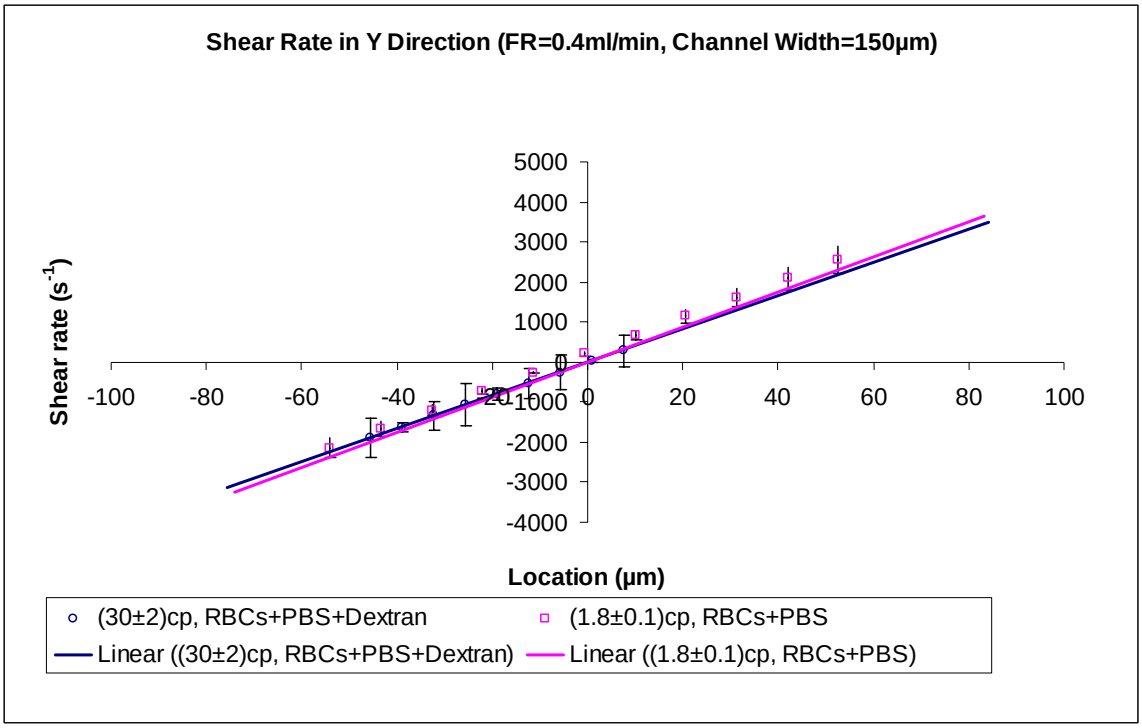

Fig. 19 Shear rate comparison between two samples, in a channel with 150µm width, channel walls are at y=-75µm and y=75µm, solid lines indicate linear regression

3.2.2.3 Wall shear stress

Figure 20 illustrates the wall shear stress in a micro channel with a width of 150µm. When the flow rate increased to 2.0ml/min, the wall shear stress could be increased to about 240Pa.

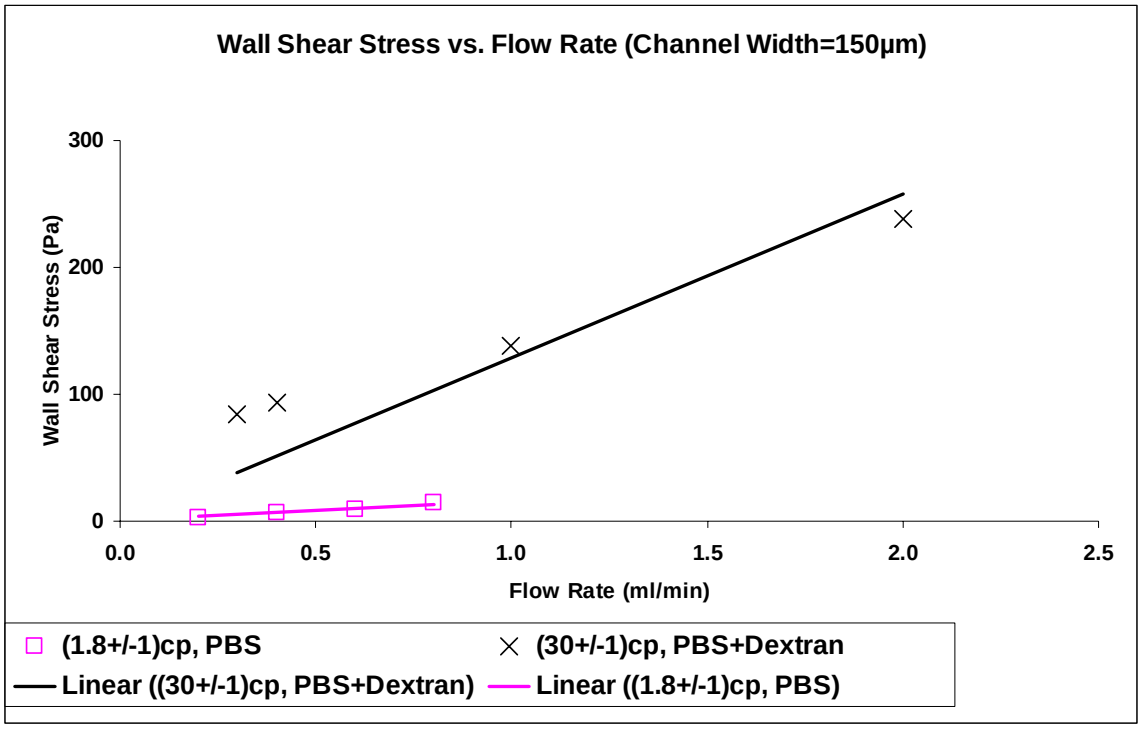

Fig. 20 Wall shear stress, in channel with 150µm width, solid lines indicate linear regression

3.2.3 At Inlet

The two-dimensional velocity in the x direction was showed in figure 21. Along the centerline, V_x increased near linearly from -118µm to 64µm (R^2=0.96), while V_y remained around zero. Along the wall, Both V_x and V_y started from a non-zero value, increased outside channel, had the

maximal values at x=0μm and decreased when the cells entered micro channel. V_y was decreased all the way down to zero.

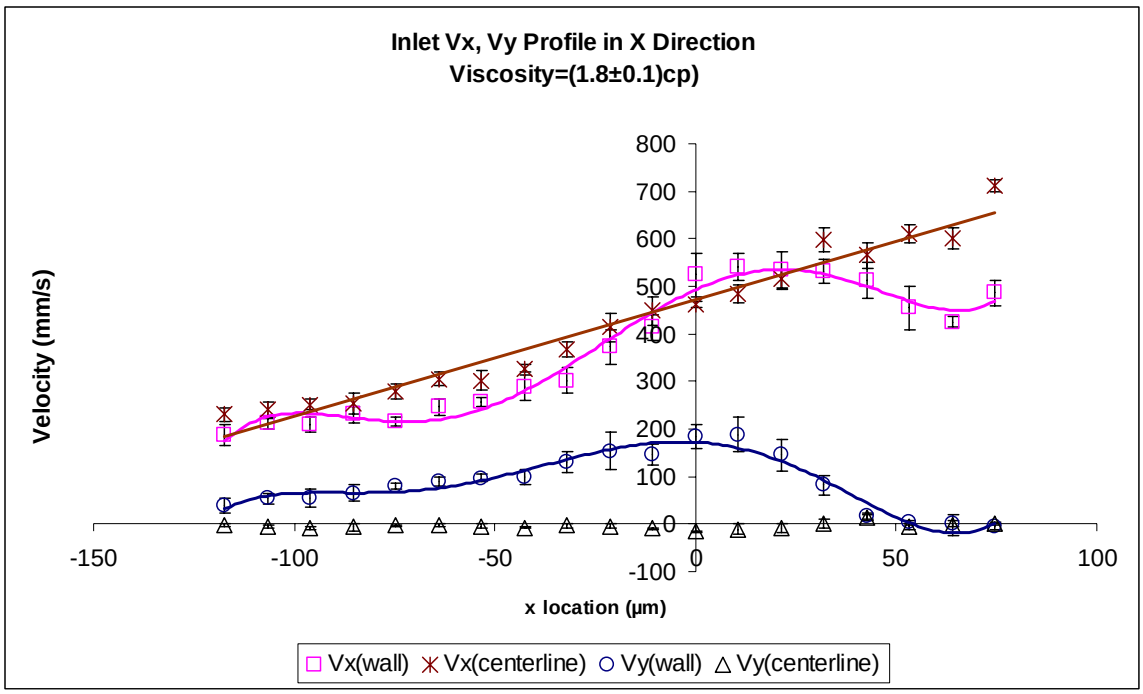

(a)

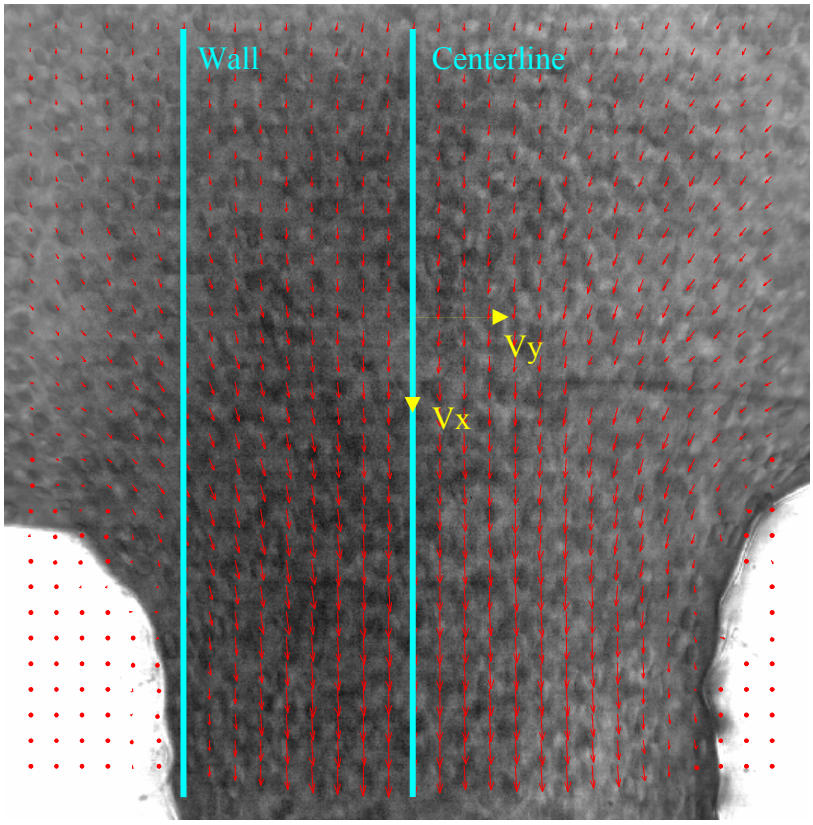

(b)

Fig. 21 Inlet velocity distribution in x direction, a: distribution, b: the location which velocity distribution is taken from, in channel with 150μm width, the solid lines on Vx(wall) and Vy(wall) indicate 5th order polynomial regression, the solid line on Vx(centerline) indicate linear regression

From 118μm outside the micro channel to 64μm inside the channel, the velocity on x direction developed from a constant value crossing y direction to a non-fully developed Poiseuille flow. The centerline shear stress remained as zero (fig.22a).

For V_y, there was a slight convergence at x=-118μm. The flow continued to aggregate as it moving towards inlet. After inlet, the V_y decreased to zero across channel width (fig.22b).

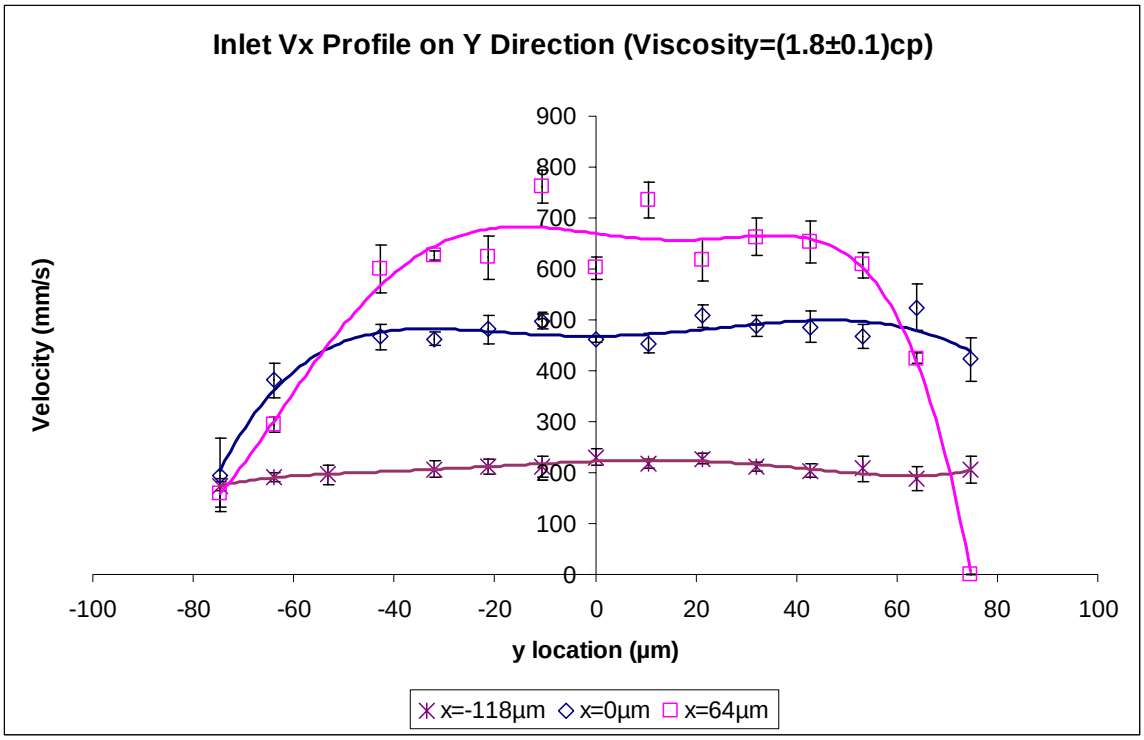
Inlet Vx Profile on Y Direction (Viscosity=(1.8±0.1)cp)
Velocity (mm/s)
900
800
700
600
500
400
300
200
100
0
-100
-80
-60
-40
-20
0
20
40
60
80
100
y location (μm)
x=-118μm
x=0μm
x=64μm

(a)

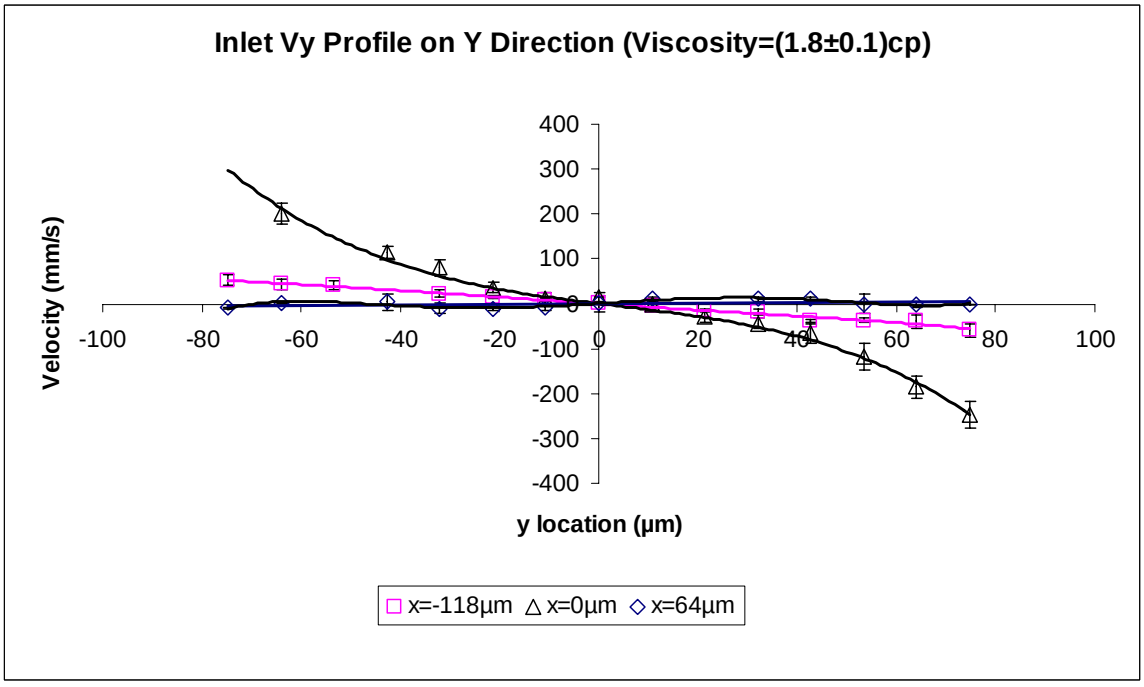
Inlet Vy Profile on Y Direction (Viscosity=(1.8±0.1)cp)
Velocity (mm/s)
400
300
200
100
0
-100
-200
-300
-400
-100
-80
-60
-40
-20
0
20
40
60
80
100
y location (μm)
x=-118μm
x=0μm
x=64μm

(b)

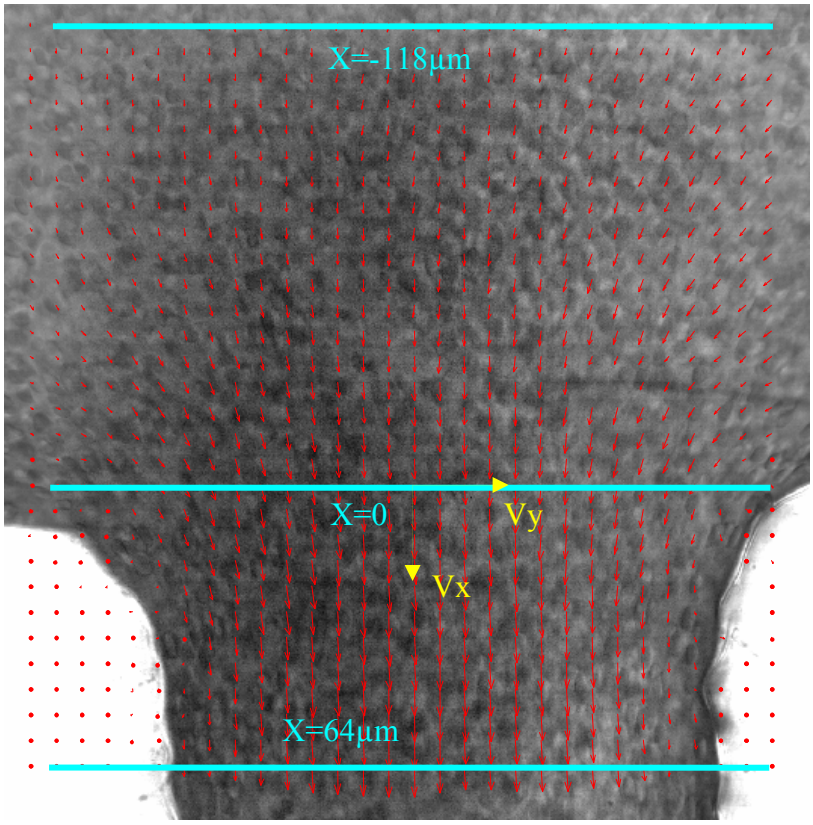

(c)

Fig. 22 Inlet velocity distribution in y direction, a: V_x distribution, b: V_y distribution c: the location which velocity distribution is taken from, in channel with 150μm width, the solid lines indicate 5^{th} order polynomial regression, channel walls are at y=-75μm and y=75μm

3.3 CELL DEFORMATION

3.3.1 Cell deformation history

In the image processing, many cells were chosen in each of the ten images taken in each of the 30 locations and the mean cell deformation was calculated. Figure 23 shows the cell deformation along the x direction when it was in a 50μm wide channel. It showed that the cell elongated gradually, reaching a maximum at approximate 0.36mm in front of the inlet. In this area, the overall elongation rate as the change of distance, which is the slope of the linear regression from point 1 to point 9, is 0.71μm/mm. At channel inlet, the elongation rate changed dramatically to 8.39μm/mm. The cell length changed from 8.04μm at point 9 to 11.48μm at point 11. A peak mean value occurred at the 11^{th} point, which is the 1^{st} point after cell entering inlet. Inside channel, which is from point 11 to point 20, the overall elongation rate is -0.26μm/mm. At the outlet of the channel, from point 20 to point 22, cell length rapidly recovered. The mean cell length from point 22 to point 30 is 6.72μm, slightly smaller than 7.18μm, which is the mean value from point 1 to point 9.

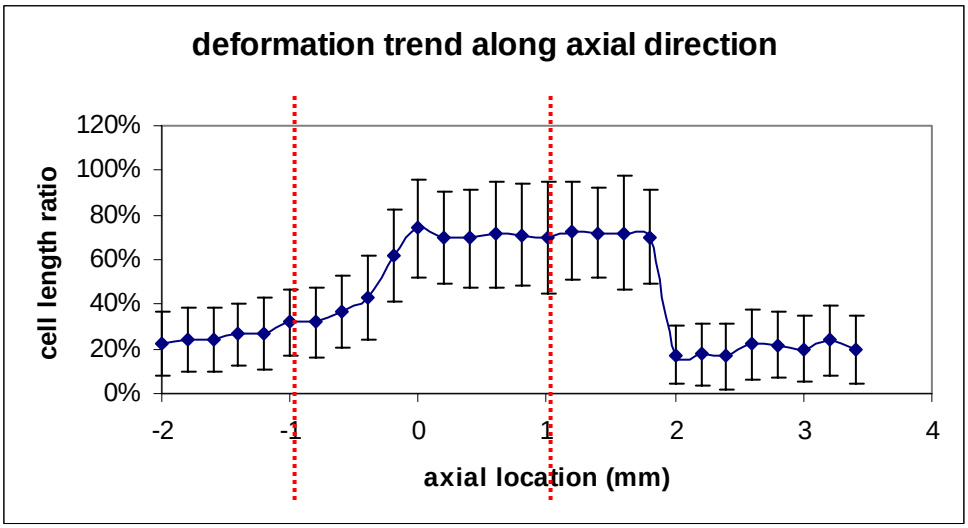

Fig. 23 Cell deformation on x direction, flow rate=0.05ml/min, inlet: x=0, outlet: x=2mm

3.3.2 Cell deformation with changing of flow rate

Figure 24 indicates the cell deformation along x dimension for three different flow rates. Table 4 shows the deformation rate, which is the slope of 1st order regression curve when cells are before inlet, at inlet, inside channel, at outlet and out of outlet. Table3 also shows the mean cell elongations before inlet, inside channel and out of outlet.

The cell deformation in individual flow ratse is similar to the result shown in figure 23. When cells are outside the channel, the elongations are increased with the increase of flow rate. The cell length before inlet is a little bit larger than the one after outlet in each flow rate. However, when cells flowed inside channel, their lengths are approximately the same in three flow rate.

As we further increase the flow rate to 2.0ml/min, the cell deformation still remained in a value between 9μm to 10μm while the velocity is proportional to flow rate.

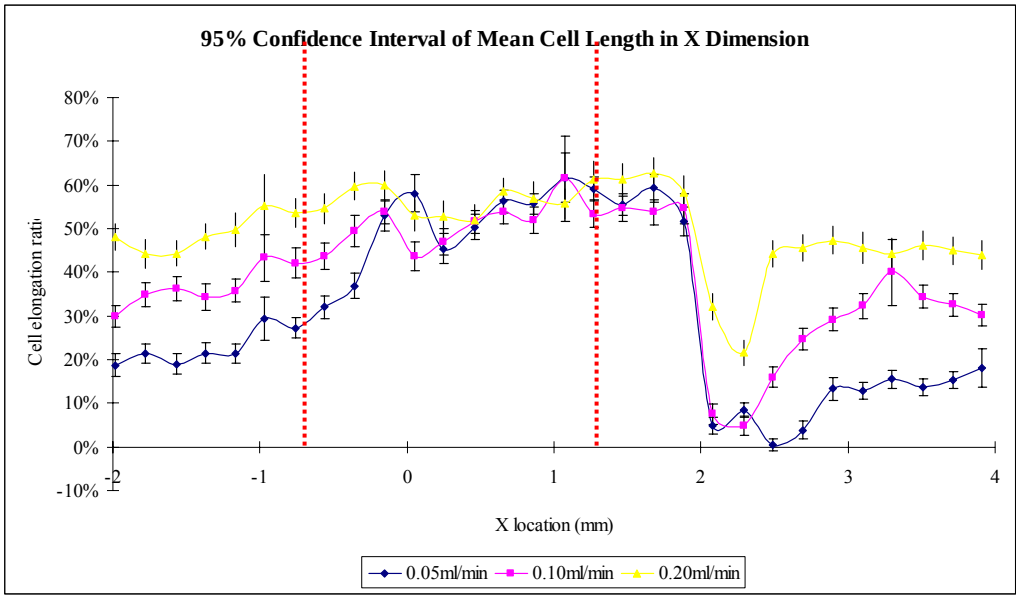

Fig. 24 Cell deformation on x direction as flow rate changes, inlet: x=0, outlet: x=2mm

Table 4 Cell deformation data

Flow rate ml/min		0.050		0.100		0.200	
Point number	distance from inlet (mm)	deformation rate (μm/mm)	mean length (μm)	deformation rate (μm/mm)	mean length (μm)	deformation rate (μm/mm)	mean length (μm)
1~9	-1.98~-0.36	0.640	7.518	0.610	8.329	0.510	9.051
9~10	-0.36~-0.15	4.600		1.250		0.020	
11~20	0.05~1.88	0.150	9.317	0.300	9.156	0.300	9.432
20~21	1.88~2.08	-14.040		-14.110		-7.830	
22~30	2.29~3.91	0.520	6.677	0.900	7.626	0.440	8.557

3.3.3 Cell deformation at inlet

Figure 25 shows cell deformation at inlet of a 50μm channel. The image was separated to four areas, in which a1 and a2 were denoted as the area near walls, b was denoted as the area around centerline inside channel and c was denoted as the area around centerline outside channel. It shows that area b had the largest deformation.

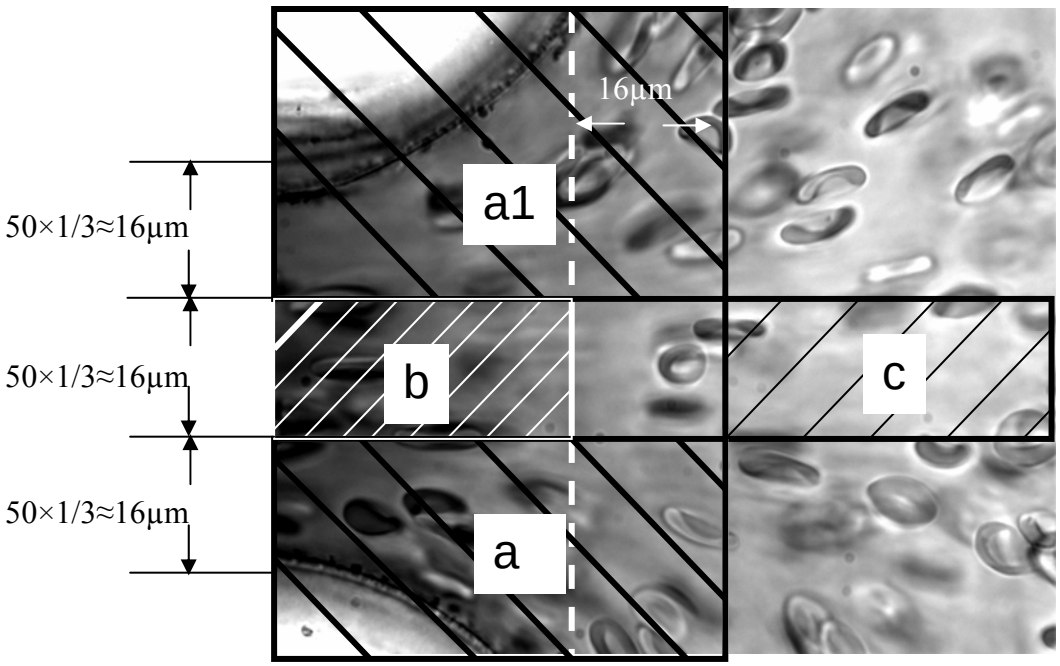

Fig. 25 Cell deformation at inlet

Table 5 Cell deformation in four areas

Area	X ends (μm)		Y ends (μm)		Cell numbers n	elongation	std
a1	-16	30	35	8	38	38.1%	23.6%
a2	-16	30	-8	8	28	36.9%	16.2%
b	-16	30	-8	-35	22	52.2%	28.0%
c	-60	-16	-8	8	22	17.4%	17.1%

3.3.4 Cell deformation orientation

With comparing figure 26a with figure 26c and comparing figure 26b with figure 26d, we can see that cell deformed parallel to the flow direction, both at inlet and inside channel. Our results are coincident with the results of Fischer et al. [11] and [12]. From the velocity profile inside channel (fig.26d), we can see a cell migration towards centerline.

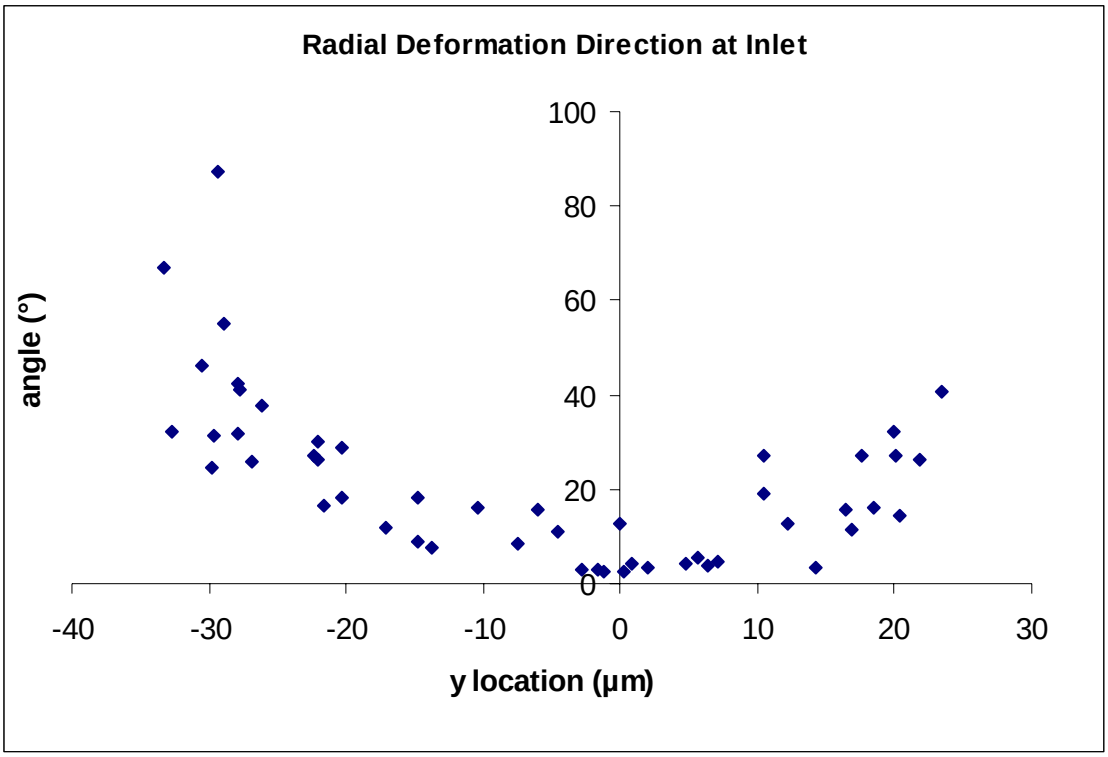
Radial Deformation Direction at Inlet
angle (°)
100
80
60
40
20
0
-40
-30
-20
-10
0
10
20
30
y location (µm)

(a)

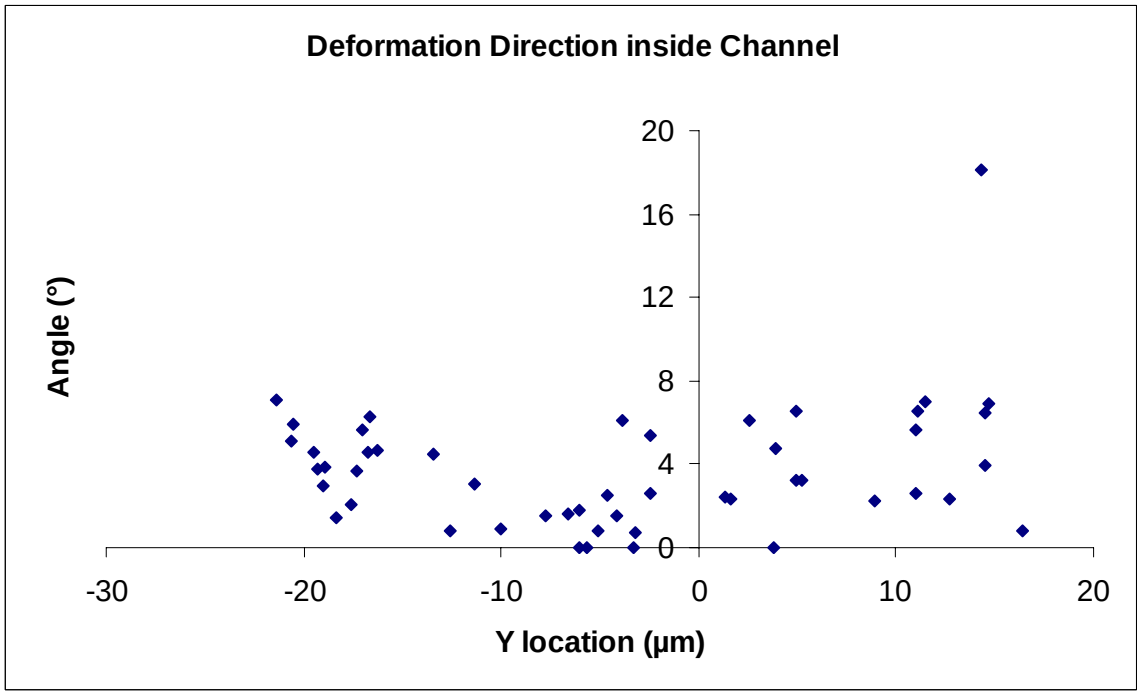
Deformation Direction inside Channel
Angle (°)
20
16
12
8
4
0
-30
-20
-10
0
10
20
Y location (µm)

(b)

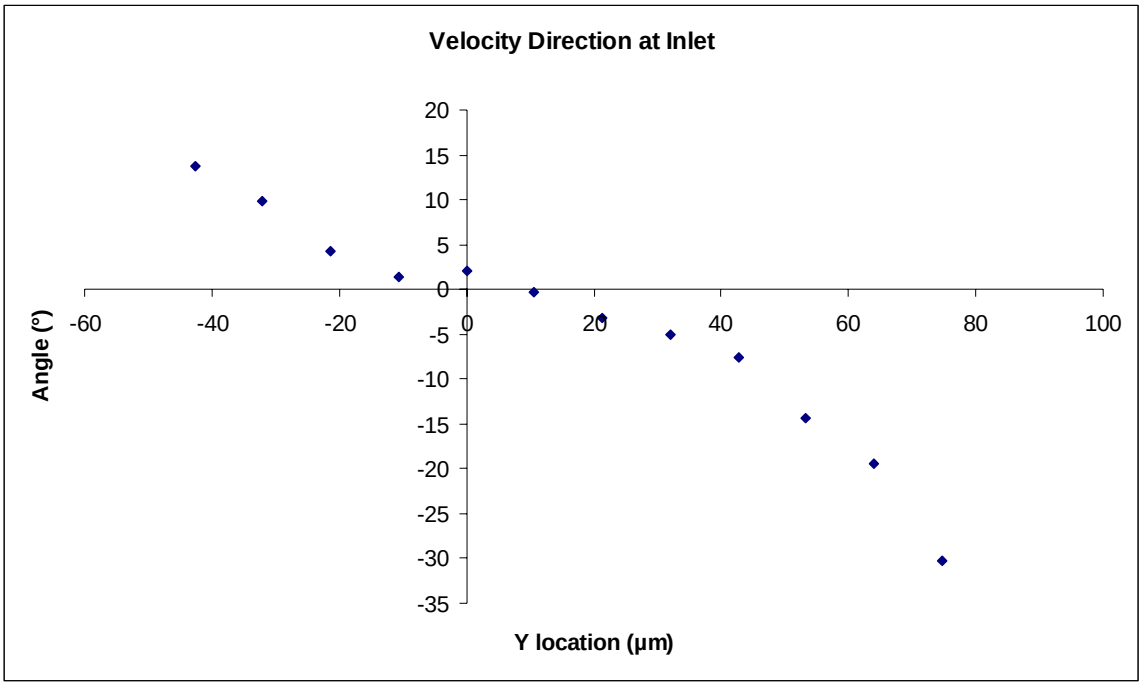

(c)

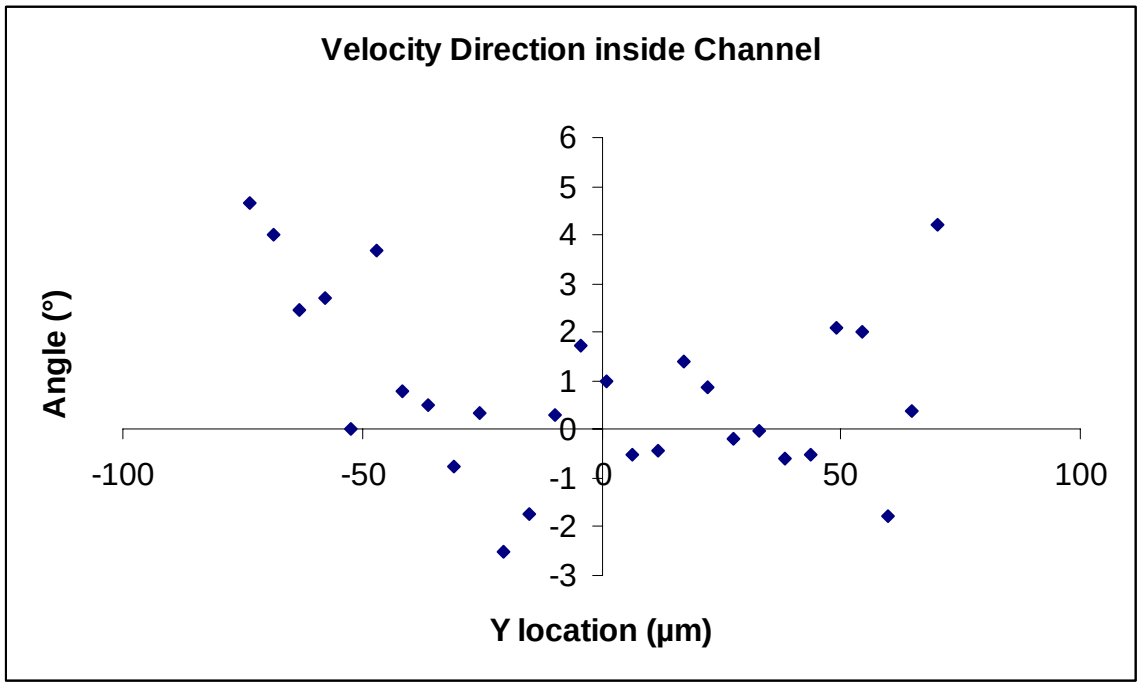

(d)

Fig. 26 Deformation and velocity direction, a: deformation direction at inlet, b: deformation direction inside channel, c: velocity direction at inlet, d: deformation direction inside channel

4.0 DISCUSSION

4.1 TWO PHASE FLOW

When blood flows through a duct whose hydraulic diameter is comparable to the diameter of red blood cells (<200μm), the two-phase composition of blood cannot be ignored. In vitro and in vivo studies have reported unique phenomena due to two-phase flow effect, such as Fahraeus-Lindquist effect near the plasma free layer [50] [51] [52] and a blunted velocity profile [53]. Blood flow in small vessels is typified by a central core of red blood cells and a cell-free layer surrounding the core.

The results presented in the previous chapter (fig.27) shows that the velocity profile across y direction fits a parabolic curve, for both low viscosity sample (R^2>0.98) and high viscosity sample (R^2>0.98). The results are consistent with the mathematical model established by Sharan and Popel [54]. They concluded that the bluntness of the velocity profile in the core was inversely related to the diameter of the tube and was direcyly related to the hematocrit. They used a parameter B to represent bluntness, with an extreme value of B→1 for a parabolic profile. For a tube with 150μm diameter, the bluntness parameter is more than 0.95 for a blood sample with 20% hematocrit. For the high viscosity sample, B will be even higher due to the hematocrit being as low as 5%.

The bluntness due to the cross section geometry can be negligible, as shown in previously.

Between two samples, the velocity is slower in the low viscosity sample, with a hematocrit of 20%. A reason for this phenomenon is the hematocrit difference. The high hematocrit sample has more cells and involves more dissipation of energy due to inelastic cell collisions. Cell deformation and centerline migration may also be reasons for the increase of velocity and wall shear rate (fig.19). At the same flow rate, the shear stress on the cells in the high viscosity samples is much larger than the one on the low viscosity samples. The cell elongation is much higher in the high viscosity sample as shown in figure 28. The cell shows an elongation parallel to flow direction,, and based on the assumption of incompressibility, the dimension normal to flow direction becomes shorter. Both of the cell deformation and cell motion will reduce the cell resistance to the flow, thus to increase the velocity and flow rate.

Another reason for this phenomenon may be the cell free layer present in the flow. The cell free layer thickness is known to increase as the hematocrit decreases [54]. This enlargement causes the image plane for the high viscosity, low hematocrit sample to be higher than the plane for the low viscosity, high hematocrit sample. As in a duct with square cross section area, the velocity will be higher as the image plane moves towards centerline.

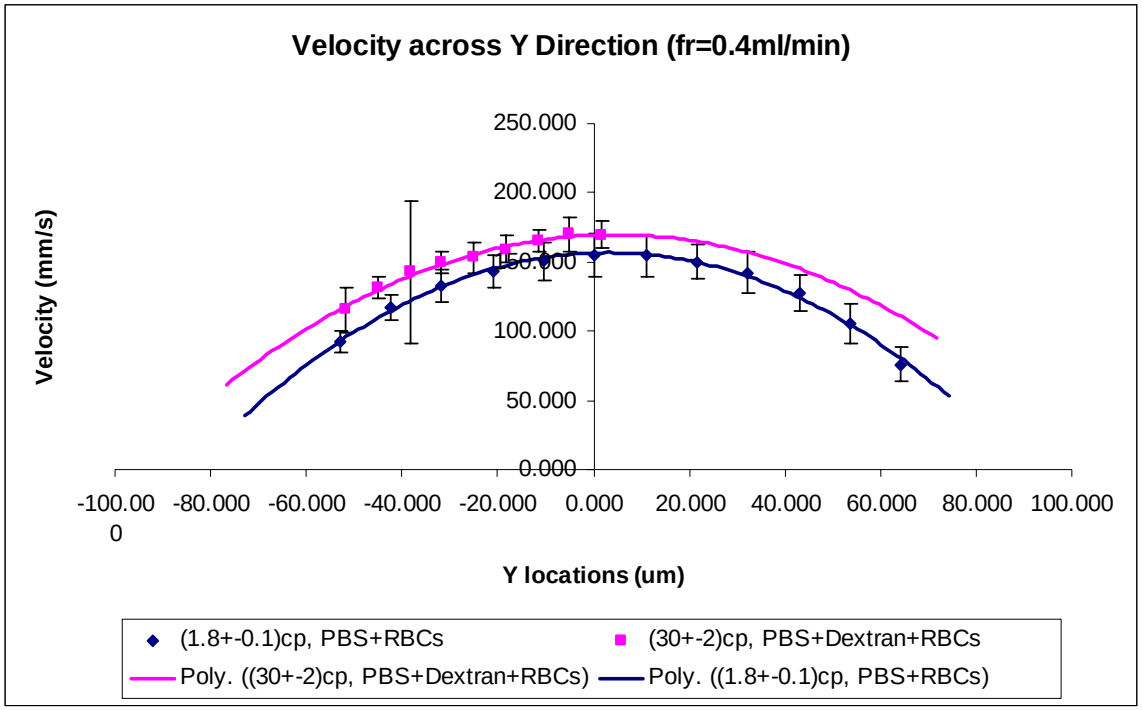

Fig. 27 Effect of viscosity on velocity profile in micro channel

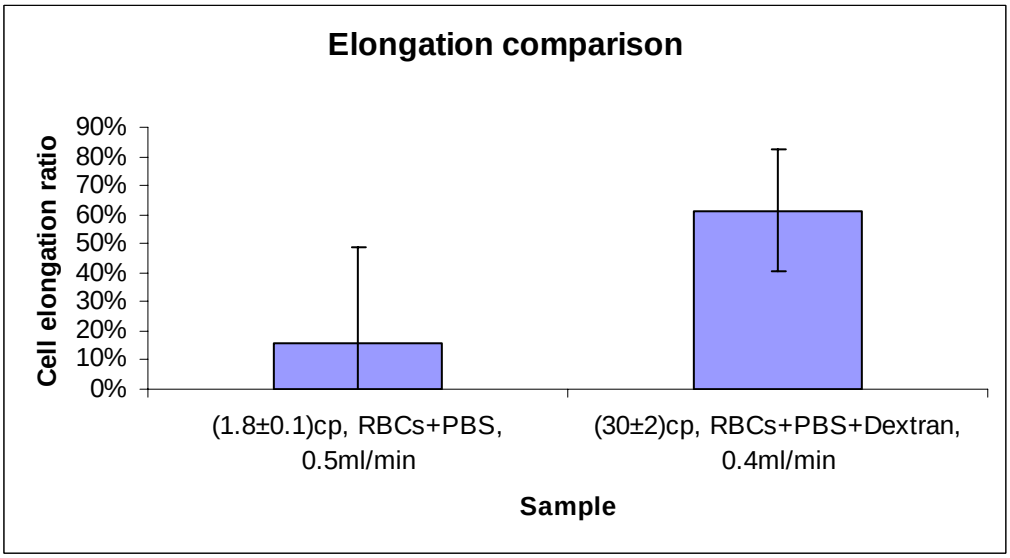

Fig. 28 Effect of viscosity on cell elongation in micro channel

4.2 INLET FLOW

The contraction flow at the channel inlet is extremely important for cell deformation and damage. However, few previous experimental reports describe the micro fluid dynamics under these conditions. Our experiments using micro fabrication technique allows us to elucidate the details of this flow field.

From the definition of extensional flow model we can see that V_x is only a function of x and V_y is only the function of y. For the velocity changes on x direction $\frac{dV}{dx}$, the y component of velocity remains as a constant. The same situation happens on y direction for $\frac{dV}{dy}$, with the x component remaining the same.

The velocity gradients observed along the centerline in our channel, with a 40:3 contraction inlet, was nearly linear in the x-direction – consistent with the property of extensional flow. Figure 22(a) also shows that for the middle 1/3 of the channel width, V_x does not change in y direction. Furthermore, at the location of x=-118μm, upstream from the throat of the contraction, there was observed a linear gradient of V_y with constant V_x, illustrating a pure extensional status. For x=64μm, the velocity profile changes to a plug flow, with a near zero y velocity component. Consequently, the extensional effect diminishes as cells flow into channel. The flow proceeds to be fully developed when it moves further into the channel. It shows there is a maximal velocity change near the corner of channel inlet. The maximal stress is located here. The centerline also showed a stress increase at inlet.

The flow pattern along wall in y direction and the flow pattern at inlet in x direction are more complex. We believe in y direction, there is a shear force due to the interaction between flow and the edge perpendicular to the channel wall, which forces the velocity direction to be altered, with a decrease of V_x and increase of V_y.

CFD results by solving Navior-Stokes equation also support this analysis. We use FEMLAB (COMSOL, Inc., Los Angels, CA), a CFD software, to illustrate the flow conditions under the same experimental situation. For the purpose of comparison, figure 29a and figure 29b are calculated without including z direction component, because experimental data can not illustrate the z direction velocity component from images taken from xy plane. The results are consistent with experimental data, with a maximal value at the corner and strong effect on centerline of extensional stress (fig.29a). Shear stress has stronger effect on the wall when z component has not been involved.

CFD also allows us to calculate the stress value which is including z component. The extensional stress is almost the same in figure29a and figure29c. However, the shear stress has great effect from the top and bottom surface, especially on the centerline inside channel.

We can summarize that at the inlet, the flow is affected by the combine effect of extensional stress and shear stress. Figure29e shows the combined effect of shear stress and extensional stress.

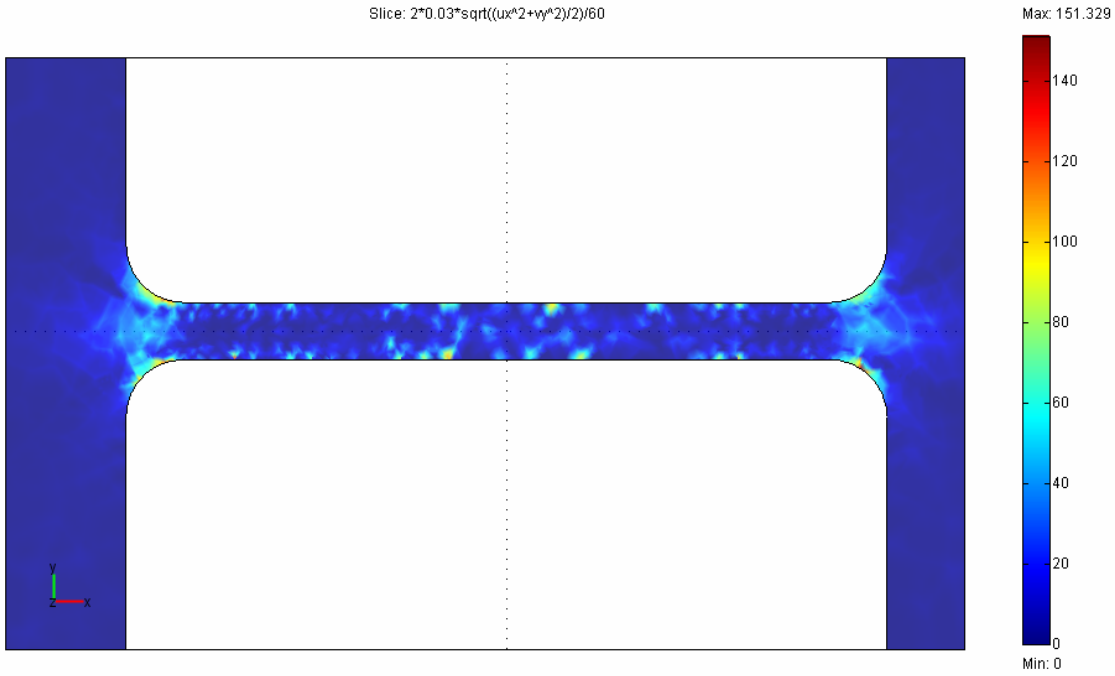
Slice: 2*0.03*sqrt((ux^2+vy^2)/2)/60
Max: 151.329
140
120
100
80
60
40
20
0
Min: 0

(a)

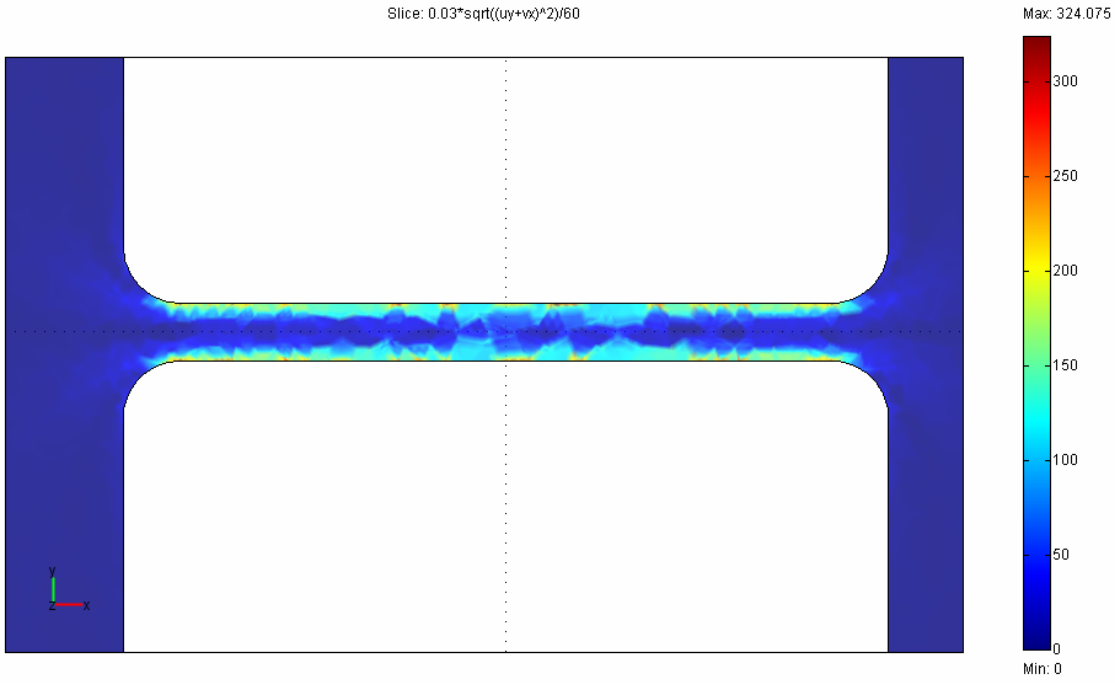
Slice: 0.03*sqrt((uy+vx)^2)/60
Max: 324.075
300
250
200
150
100
50
0
Min: 0

(b)

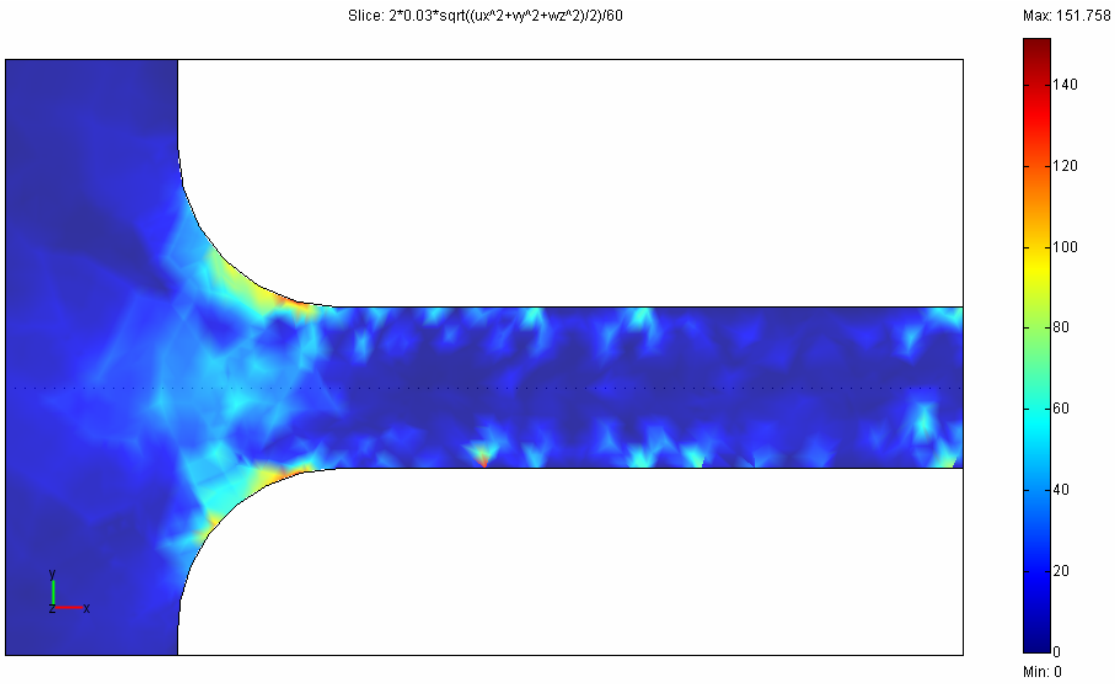
Slice: 2*0.03*sqrt((ux^2+vy^2+wz^2)/2)/60
Max: 151.758
140
120
100
80
60
40
20
0
Min: 0
y
z
x

(c)

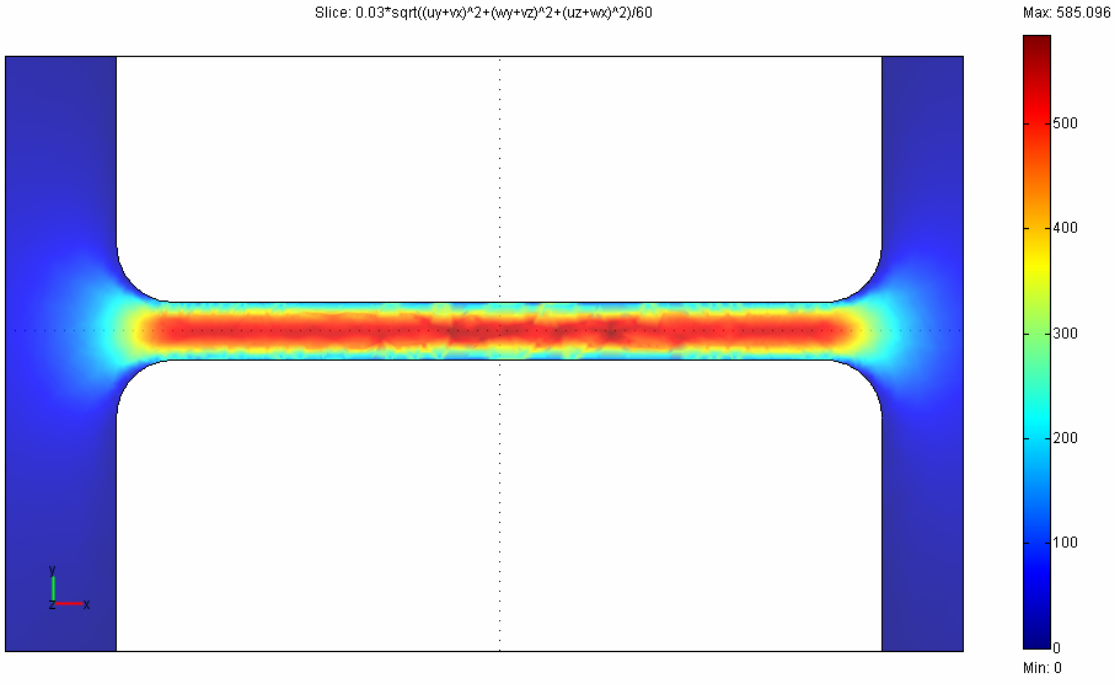
Slice: 0.03*sqrt((uy+vx)^2+(wy+vz)^2+(uz+wx)^2)/60
Max: 585.096
500
400
300
200
100
0
Min: 0
y
z
x

(d)

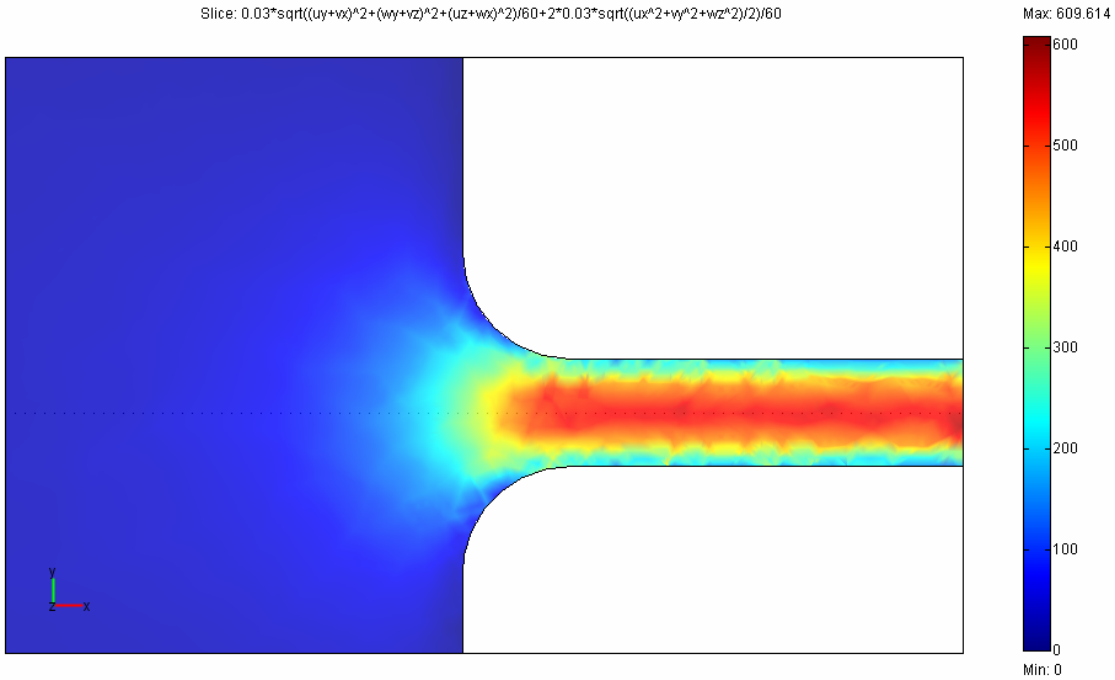

(e)

Fig. 29 CFD results of inlet flow conditions, flow rate=0.5ml/min, viscosity=30cp, channel width=150μm, (a): extensional stress w/o z component, (b); shear stress w/o z component, (c): extensional stress w/ z component, (d): shear stress w/ z component, (e): extensional stress and shear stress w/ z component,

The cell deformation profiles observed these studies revealed that the largest deformation occurs at the inlet, surrounding the centerline for 1/3 of the channel width. We believe the maximum deformation at inlet is induced by the combine effect of extensional stress and shear stress.

4.3 CELL DEFORMATION

The cell deformation history shows that the cells deform dramatically near inlet, bearing maximum elongation at inlet and recovering as soon as they flow out of the outlet.

4.3.1 Deformation at inlet

We believe the maximum deformation at the inlet is induced by the combined effect extensional stress and shear stress. When blood becomes a duct flow, the elongational effect is substituted by shear stress. When pure shear stress acts on cells, cell elongation decrease only slightly.

4.3.2 Deformation at outlet

At the outlet, cells are found to recover as soon as they exit the channel. That result is quite different from the observation of Sutera et al., which showed a period of about 1 minute for recovery. The reason should be the different exposure time in the two experiments. We conclude that a cell can recover as soon as stress is unloaded after a short exposure time (on the order of micro seconds), but needs some extra time to recover after being exposed to a stress for a longer time (in minutes).

The CFD results show that the rapid decrease of cell deformation could because of the sudden vanish of shear stress, as shown in figure 30(a). There is also showed a rotation of flow at exit, which cause the cell stagnant at exit area and is smaller than the one afterwards.

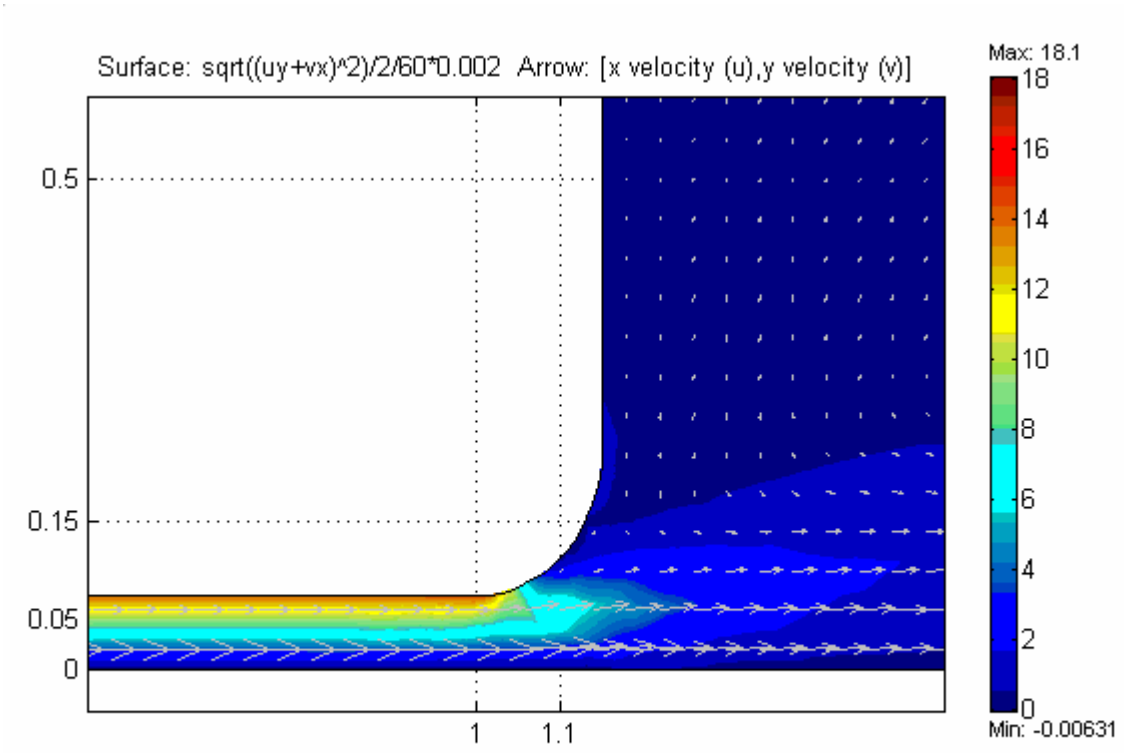

Fig. 30 shear stress and velocity at outlet, flow rate=0.5ml/min, viscosity=2cp, channel width=150μm

After cells exit, they enter a duct which has a diameter that is much wider than the micro channel. However the net shear dv_x/dy is virtually the same as the upstream duct. This shear stress is however small and does not influence the deformation on the cell. The deformation is the same as the one before inlet.

At outlet, cell recovers to a diameter which is shorter than the one after exit. The decreased diameter is the result of pure extensional stress.

The results of cell deformation over the x direction are consistent with the macro scale results of Umezu's experiment [34]. In his study, hemolysis was tested in different types of stenosis in a flow loop. The hemolysis in a stenosis with abrupt inlet and tapered outlet is 3 times greater than the one with a tapered inlet and abrupt outlet. Because abrupt connectors caused more hemolysis than tapered ones, we can conclude that the inlet geometry is more important in affecting hemolysis. We found the same phenomenon from our experiment, in which cell bore its maximum deformation at inlet.

4.4 EFFECT OF FLOW RATE

When flow rate increases, the cell deformation outside channel increased proportionally to the increasing velocity. However, the cells inside the channel demonstrated no further deformation above an asymptotic value, which in this case was 9.91μm in length or 155% of the original diameter (fig.31).

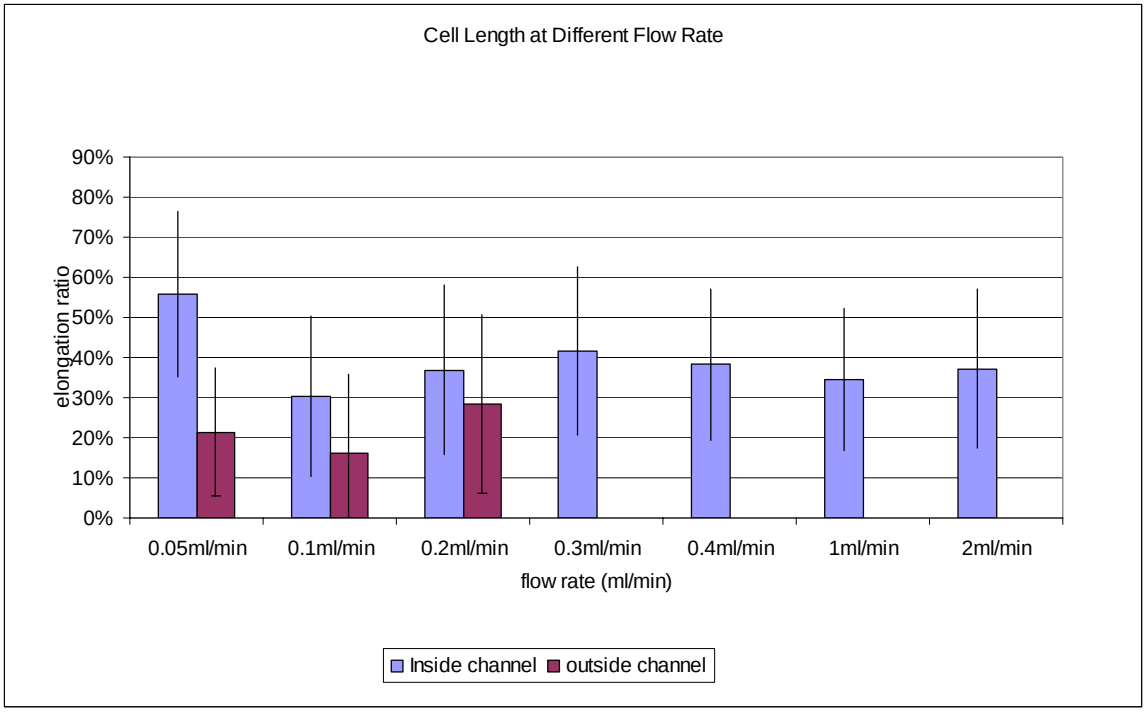

Fig. 31 Cell deformation inside and outside the channel

Figure 32 shows a summarized relationship of wall shear stress of channel and cell deformation ratio in our experiment. The wall shear stress is calculated from theoretical equation (equation 2). Cell is sensitive to low shear stress from 0 to 10^{-2} Pa. It will reach to a threshold when shear stress extends 10^{-2} Pa, and stay at this threshold as shear stress increases from 10^{-2} Pa to 10^{2}-10^{3} Pa.

One explanation for this phenomenon is the elasticity of the cell membrane. A blood cell is sensitive to shear stress and will readily to elongate when exposed to low shear stress. However, as the shear stress increasing, the cell membrane may reach a threshold and stop further elongation, due to the limitation of cell surface area and volume[55] [56] [57]. The measured

critical areal strain is 2-3%, beyond which the cell will be ruptured. A critical membrane tension of 10^{-2} N/m is needed to cause cell rupture. However, a membrane tension of 10^{-5}-10^{-7}, which is much lower than the critical value, can cause the generation of pores on cell membrane, which may result in the sublethal blood damage[56] [58].

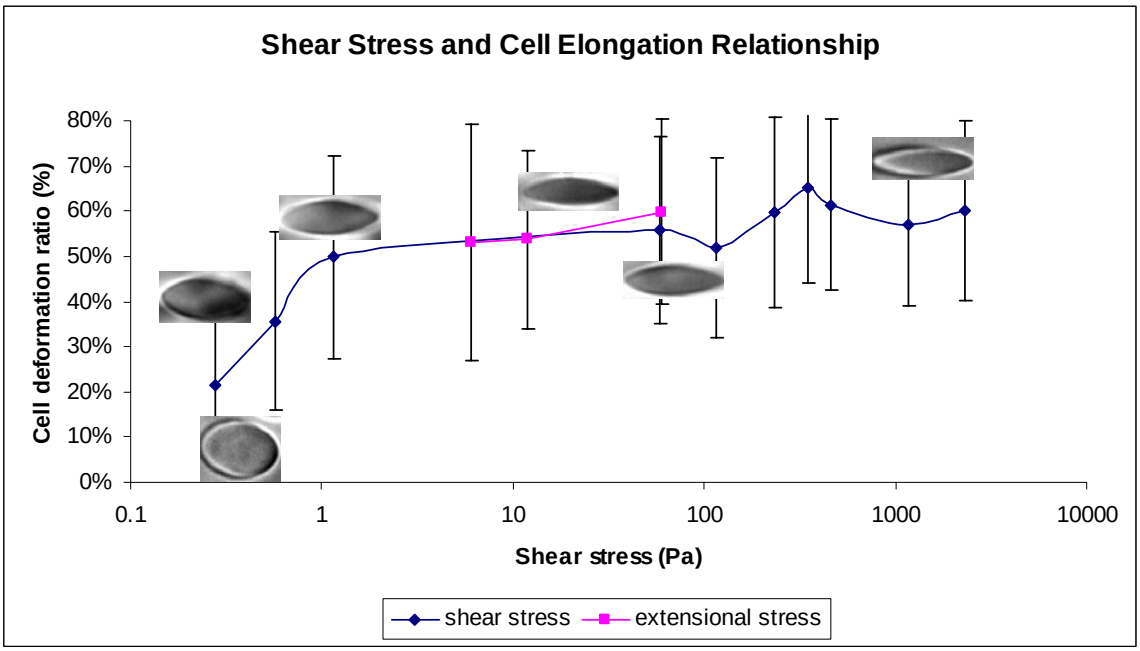

Fig. 32 Relationship of stress and cell elongation, shear stress and extensional stress are calculated from CFD results

The membrane tension is calculated using the method established by Lokhandwalla et al. [58], assuming a steady flow conditions. In their paper, cell deformation was separated to two catalogs: inertial mode, where cell membrane elastic tension is less than the inertial forces generated by surrounding fluid, and viscous mode, where membrane elastic tension is greater than the inertial forces. In viscous mode, the tangential viscous stresses are exerted on the wall and be in equilibrium with membrane elastic tension, $T_{elas} \approx T_{visc}$. In inertial mode, viscous stress

is near zero ($T_{visc} \approx 0$). The equations for calculating T_{iner} and T_{visc} in steady flow were give in the paper:

$$T_{iner} = \rho r_c^3 k^2 \quad (21)$$

$$T_{visc} = \mu k r_c \quad (22)$$

Where, ρ and μ are the density and viscosity of flow, respectively; r_c is the radius of red blood cells and k is shear rate.

Our results also shows the cell is in the viscous mode described in their paper, where inertial tension from flow are smaller than the cell membrane elastic tension. The largest membrane tension we can achieve is on the order of 10^{-3}-10^{-2}, which is much lower than the critical tension to rupture cells but large enough to change the cell membrane feature.

At the inlet, the cell has a larger deformation than inside channel. However, the cell exposure time for the extensional flow is much shorter than the cell exposure time for shear flow. We conclude that the combine effects of extensional stress and shear stress can cause larger deformation in a shorter time.

5.0 CONCLUSION

An experimental investigation was undertaken to study the cellular dynamics that occurs at "hot-spots" in cardiovascular devices which feature non-uniform high shear stress conditions and are primarily responsible for hemolysis. The flow and cell deformation fields of blood cells were recorded within micro channels in vitro. We conclude that 1) when cells flow through a small gap or clearance, they successively bear a pure extensional stress, a combined effect of extensional stress and shear stress, a pure shear stress, and the unloading of extensional stress and shear stress. 2) cells deform to maximum in a transient time under the combined effect of extensional stress and shear stress when they enter the gap or clearance; 3) the largest possibility for blood damage occurs at the inlet of gaps or clearance; 4) the relationship of cell deformation and shear stress illustrates that cell is sensitive to low shear stress and stay in a threshold at high shear stress; 5) after bearing a high shear stress for a short exposure time, cells recover as soon as stress is relieved; 6) The sublethal damage is more likely to happen than the visible rupture of cells under the situation of "hot-spots**".**

6.0 FUTURE WORK

Our findings for the blood damage conditions at “hot-spots” show basic mechanism underlining device-induced blood damage. The methods are proved to be effective and are ready to be applied in further design and optimization. In the future, the investigation can be performed on the following tracks: 1) investigate cell damage in more complex flow conditions; 2) apply the experimental results in the design and optimization of “hot-spots” geometry; 3) Investigate the device effects on pathological cells; 4) investigate the basic mechanism of thrombosis at “hot-spots”.

APPENDIX A

CELL DEFORMATION AND LOCATION

```
%%This program is to get the cell deformation and location information
clear,close all;
name=input('the root name of the image?', 's');
time=input('separate time?');
fid=fopen([name '_deformation.txt'],'a');
fprintf(fid,'name of the file= %s \n',name);
fprintf(fid,'separation time= %4d \n',time);
fprintf(fid,'center_x, center_y, length, length_x, length_y (pixel)\n');
for i=1:2:19
    if i<=9                              %read the set of two pictures
       im=imread([name '\' name '_00' int2str(i) '.tif']);
    else
       im=imread([name '\' name '_0' int2str(i) '.tif']);
    end
    imshow(im);
    g=ginput;
    L=length(g);
    for p=1:2:(L-1)
       center((p+1)./2,1)=(g(p,1)+g((p+1),1))./2;
       center((p+1)./2,2)=(g(p,2)+g((p+1),2))./2;
       leng((p+1)./2)=sqrt((g(p,1)-g((p+1),1)).^2+(g(p,2)-g((p+1),2)).^2);
       lxy((p+1)./2,1)=abs(g(p,1)-g((p+1),1));
       lxy((p+1)./2,2)=abs(g(p,2)-g((p+1),2));
       data1=center((p+1)./2,1);
       data2=center((p+1)./2,2);
       data3=leng((p+1)./2);
       data4=lxy((p+1)./2,1);
       data5=lxy((p+1)./2,2);
       fprintf(fid, '%10.3f, %10.3f, %10.3f, %10.3f, %10.3f\n', data1,data2,data3,data4,data5);
    end
end
```

```
fopen([name '_deformation.txt'],'r');
```

APPENDIX B

MEAN AND STANDARD DEVIATION

```
%This function is to get the mean and standard deviation of x values at
%fixed y location.
%lox=x location; loy=y location;vx=velocity of x direction; vy=velocity of
%y direction;
function [mn,sd]=sdvec(name);
file=importdata([name '.vec']);     %load .vec file
data=file.data;                     %load data part of the file
lox=data(:,1);
loy=data(:,2);
vx=data(:,3);
vy=data(:,4);
j=1;
for i=132:64:900
   ii=find(loy==i);
   fx=vx(ii);          %find vx at the location of particular y value.
   fy=vy(ii);
   iii=find(fx);       %find fx which is not equal to zero
   nonzerofx=fx(iii);
   nonzerofy=fy(iii);
   iv=find((atan(nonzerofy./nonzerofx).*180./3.14)<10);
   ffx=nonzerofx(iv);
   mn(j,1:2)=[i,mean(ffx)];    %mean and sd are both j*2 matrices
   sd(j,1:2)=[i,std(ffx)];
   j=j+1;
end



%%Main program
clear,close all;
name=input('the root name of the files?', 's');
```

```
n=input('the last file number?','s');
time=input('separate time?');                    %input separation time, unit 'us'
fid=fopen([name '_mean and sd.txt'],'a');
fprintf(fid,'file name: %s\n',name);
fprintf(fid,'separate time: %4d us\n',time);
fprintf(fid,'loc_Y, Mean_X_D, STD_X_D, \n');
for i=1:2:n
   if i<=9
      NM=[name '_00' int2str(i)];
   else
      NM=[name '_0' int2str(i)];
   end
[mn,sd]=sdvec(NM);      %mn means 'mean'.
loy=mn(:,1);
meanvx=mn(:,2);
sdvx=sd(:,2);
s=length(loy);
for j=1:s
fprintf(fid,'%10.3f, %10.3f, %10.3f \n',loy(j,1), meanvx(j,1), sdvx(j,1));
end
end
fid=fopen([name '_mean and sd.txt'],'r');
```

BIBLIOGRAPHY

1. Fung, Y.C., *Biomechanics, Mechanical Properties of Living Tissues*. 2nd ed. 1993, New York: Springer-Verlag New York, Inc.

2. Chien, S., Usami, S., Taylor, M., Lundberg, J. L., Gregersen, M.I., *Effects of hematocrit and plasma proteins of human blood rheology at low shear rates.* J. Appl. Physiol., 1966. **21**: p. 81-7.

3. Cokelet, G.R., Merrill, E. W., Gilliland, E. R., Shin, H., Britten, A., Wells, R. E., *The rheology of human blood measurement near and at zero shear rate.* Trans. Soc. Rheol., 1963. **7**: p. 303-17.

4. Merrill, E.W., Gilliland, E. R., Cokelet, G. R., Shin, H., Britten, A., Wells, R. E., *Rheology of human blood, near and at zero flow.* Biophys. J., 1963. **3**: p. 199-213.

5. Casson, M., *A flow equation for pigment-oil suspensions of the printing ink type*, in *Rheology of Disperse Systems*, C.C. Mills, Editor. 1959, Pergamon: Oxford. p. 84-104.

6. Chien, S., Usami, S., Dellenbeck, R. J., Gregersen, M.I., *Shear dependent deformation of erythrocytes in rheology of human blood.* Am. J. Physiol., 1970. **219**: p. 136-42.

7. Reinke, W., Johnson, P. C.,Gaehtgens, P., *Effect of shear rate variation on apparent viscosity of human blood in tubes of 29 to 94 microns diameter.* Circulation research, 1986. **59**(2): p. 124-32.

8. Reinke, W., Gaehtgens, P.,Johnson, P. C., *Blood viscosity in small tubes: effect of shear rate, aggregation, and sedimentation.* The American journal of physiology, 1987. **253(3) Pt 2**: p. H540-7.

9. Bishop, J.J., Nance, P. R.,Popel, A. S.,Intaglietta, M.,Johnson, P. C., *Erythrocyte margination and sedimentation in skeletal muscle venules.* American journal of physiology Heart and circulatory physiology, 2001. **281**(2): p. H951-8.

10. Chien, S., Feng, S. S.,Vayo, M.,Sung, L. A.,Usami, S.,Skalak, R., *The dynamics of shear disaggregation of red blood cells in a flow channel.* Biorheology, 1990. **27**(2): p. 135-47.

11. Fischer, T., Schmid-Schonbein, H., *Tank tread motion of red cell membranes in viscometric flow: behavior of intracellular and extracellular markers (with film).* Blood cells, 1977. **3**: p. 351-65.

12. Sutera, S.P., Mehrjardi, M., Mohandas, N., *Deformation of erythrocytes under shear.* Blood cells, 1975. **1**: p. 369-74.

13. Blackshear, P.L., *Mechanical hemolysis in flow blood*, in *Biomechanics: its foundatrion and objectives*, Y.C. Fung, Editor. 1972, Prentice Hall: Englewood Cliffs, NJ. p. 501-27.
14. Hellums, J.D., Brown, C. L., *Blood cell damage by mechanical forces*, in *Cardiovascular flow dynamics and measurements*, N.H. Hwang, Norman, N. A., Editor. 1977, University Park Press: Baltimore. p. 799-823.

15. Sutera, S.P., *Flow-induced trauma to blood cells.* Circ Res, 1977. **41**(1): p. 2-8.

16. Leverett, L.B., Hellums, J. D.,Alfrey, C. P.,Lynch, E. C., *Red blood cell damage by shear stress.* Biophysical journal, 1972. **12**(3): p. 257-73.

17. Williams, A.R., Hughes, D. E., Nyborg, W. L., *Hemolysis near a transversely oscilating wire.* Science, 1970. **169**: p. 871-3.

18. Lu, P.C., Lai, H. C.,Liu, J. S., *A reevaluation and discussion on the threshold limit for hemolysis in a turbulent shear flow.* J Biomech, 2001. **34**(10): p. 1361-4.

19. Hetzer, R., Loebe, M., Potapov, E.V., *Circulatory support with pneumatic paracorporeal ventricular assist device in infants and children.* Ann Thorac Surg, 1998. **66**: p. 1498-506.

20. Akutsu, T., *Artificial heart: total replacement and partial support*. 1975, Tokyo: Igaku Shoin Ltd.

21. Burda, G., Trittenwein, H.,Carole, H.,Trittenwein, G., *Testing of extracorporeal membrane oxygenation circuit related hemolysis using long-term stored packed red cells and fresh frozen plasma.* Artif Organs, 2004. **28**(5): p. 496-9.

22. Okumiya, T., Ishikawa-Nishi, M.,Doi, T.,Kamioka, M.,Takeuchi, H.,Doi, Y.,Sugiura, T., *Evaluation of intravascular hemolysis with erythrocyte creatine in patients with cardiac valve prostheses.* Chest, 2004. **125**(6): p. 2115-20.

23. Allman, C., Rajaratnam, R.,Kachwalla, H.,Hughes, C. F.,Bannon, P.,Leung, D. Y., *An unusual cause of hemolysis in a patient with an aortic valved conduit replacement.* J Am Soc Echocardiogr, 2003. **16**(2): p. 188-90.

24. Kameneva, M.V., Undar, A.,Antaki, J. F.,Watach, M. J.,Calhoon, J. H.,Borovetz, H. S., *Decrease in red blood cell deformability caused by hypothermia, hemodilution, and mechanical stress: factors related to cardiopulmonary bypass.* Asaio J, 1999. **45**(4): p. 307-10.

25. Kameneva, M.V. *Hemorheological problems in the development of artificial organs*. in *International conference on biorheology and school fo ryoung scientists*. 2000. Sofia, Bulgaria.

26. Wu, Z.J., Shu, M. C.,Scott, D. R.,Hwang, N. H., *The closing behavior of Medtronic Hall mechanical heart valves.* Asaio J, 1994. **40**(3): p. M702-6.

27. Meyer, R.S., Deutsch, S.,Maymir, J. C.,Geselowitz, D. B.,Tarbell, J. M., *Three-component laser Doppler velocimetry measurements in the regurgitant flow region of a Bjork-Shiley monostrut mitral valve.* Ann Biomed Eng, 1997. **25**(6): p. 1081-91.

28. Lamson, T.C., Rosenberg, G.,Geselowitz, D. B.,Deutsch, S.,Stinebring, D. R.,Frangos, J. A.,Tarbell, J. M., *Relative blood damage in the three phases of a prosthetic heart valve flow cycle.* Asaio J, 1993. **39**(3): p. M626-33.

29. Wiebalck, A., Flameng, W., *Hemolysis with the F21 hemopump.* Int J Artif Organs, 1995. **18**(7): p. 365-71.

30. Anai, H., Wakisaka, Y.,Nakatani, T.,Taenaka, Y.,Takano, H.,Hadama, T., *Relationship between pump speed design and hemolysis in an axial flow blood pump.* Artif Organs, 1996. **20**(6): p. 564-7.

31. Ohashi, Y., de Andrade, A.,Nose, Y., *Hemolysis in an electromechanical driven pulsatile total artificial heart.* Artif Organs, 2003. **27**(12): p. 1089-93.

32. James, N.L., Wilkinson, C. M.,Lingard, N. L.,van der Meer, A. L.,Woodard, J. C., *Evaluation of hemolysis in the VentrAssist implantable rotary blood pump.* Artif Organs, 2003. **27**(1): p. 108-13.

33. Wu, Z.J., Antaki, J. F.,Burgreen, G. W.,Butler, K. C.,Thomas, D. C.,Griffith, B. P., *Fluid dynamic characterization of operating conditions for continuous flow blood pumps.* Asaio J, 1999. **45**(5): p. 442-9.

34. Umezu, M., Fujimasu, H., Yamada, T. *Fluid dynamic investigation of mechanical blood hemolysis*. in *The 5th international symposium on artificial heart and assist devices*. 1995. Tokyo, Japan: Springer.

35. Sharp, M.K., Mohammad, S. F., *Scaling of hemolysis in needles and catheters.* Ann Biomed Eng, 1998. **26**(5): p. 788-97.

36. Giersiepen, M., Wurzinger, L. J.,Opitz, R.,Reul, H., *Estimation of shear stress-related blood damage in heart valve prostheses--in vitro comparison of 25 aortic valves.* Int J Artif Organs, 1990. **13**(5): p. 300-6.

37. Grigioni, M., Daniele, C.,Morbiducci, U.,D'Avenio, G.,Di Benedetto, G.,Barbaro, V., *The power-law mathematical model for blood damage prediction: analytical developments and physical inconsistencies.* Artif Organs, 2004. **28**(5): p. 467-75.

38. Okamoto, E., Hashimoto, T.,Inoue, T.,Mitamura, Y., *Blood compatible design of a pulsatile blood pump using computational fluid dynamics and computer-aided design and manufacturing technology.* Artif Organs, 2003. **27**(1): p. 61-7.

39. Goubergrits, L., Affeld, K., *Numerical estimation of blood damage in artificial organs.* Artif Organs, 2004. **28**(5): p. 499-507.

40. Mitoh, A., Yano, T.,Sekine, K.,Mitamura, Y.,Okamoto, E.,Kim, D. W.,Yozu, R.,Kawada, S., *Computational fluid dynamics analysis of an intra-cardiac axial flow pump.* Artif Organs, 2003. **27**(1): p. 34-40.

41. Kato, T., Kawano, S.,Nakahashi, K.,Yambe, T.,Nitta, S.,Hashimoto, H., *Computational flow visualization in vibrating flow pump type artificial heart by unstructured grid.* Artif Organs, 2003. **27**(1): p. 41-8.

42. Yano, T., Sekine, K.,Mitoh, A.,Mitamura, Y.,Okamoto, E.,Kim, D. W.,Nishimura, I.,Murabayashi, S.,Yozu, R., *An estimation method of hemolysis within an axial flow blood pump by computational fluid dynamics analysis.* Artif Organs, 2003. **27**(10): p. 920-5.

43. Schima, H., Muller, M. R.,Papantonis, D.,Schlusche, C.,Huber, L.,Schmidt, C.,Trubel, W.,Thoma, H.,Losert, U.,Wolner, E., *Minimization of hemolysis in centrifugal blood pumps: influence of different geometries.* Int J Artif Organs, 1993. **16**(7): p. 521-9.

44. Burgreen, G.W., Antaki, J. F.,Wu, Z. J.,Holmes, A. J., *Computational fluid dynamics as a development tool for rotary blood pumps.* Artif Organs, 2001. **25**(5): p. 336-40.

45. Lee, C.S., Chandran, K. B., *Instantaneous back flow through peripheral clearance of Medtronic Hall tilting disc valve at the moment of closure.* Ann Biomed Eng, 1994. **22**(4): p. 371-80.

46. White, F.M., *Viscous Fluid Flow*. 2nd ed. 1991, New York: McGaw-Hill, Inc.

47. Duffy, D.C., McDonald, J. C., Schueller, O. J., Whitesides, G. M., *Rapid Prototyping of Microfluidic Systems in Poly(dimethylsiloxane).* Anal. Chem., 1998. **70**: p. 4974-84.

48. Morrison, F.A., *Understanding Rheology*. 2001: Oxford University Press.

49. Bird, R.B., Stewart, W.E., Lightfoot, E.N., *Transport phenomena*. 2nd ed. 2002, New York: John Wiley & Sons, Inc.

50. McKay, C.B. and H.J. Meiselman, *Osmolality-mediated Fahraeus and Fahraeus-Lindqvist effects for human RBC suspensions.* Am J Physiol, 1988. **254**(2 Pt 2): p. H238-49.

51. McKay, C.B., O. Linderkamp, and H.J. Meiselman, *Fahraeus and Fahreaus-Lindqvist effects for neonatal and adult red blood cell suspensions.* Pediatr Res, 1993. **34**(4): p. 538-43.

52. Pries, A.R. and T.W. Secomb, *Rheology of the microcirculation.* Clin Hemorheol Microcirc, 2003. **29**(3-4): p. 143-8.

53. Sirs, J.A., *The flow of human blood through capillary tubes.* J Physiol, 1991. **442**: p. 569-83.

54. Sharan, M., Popel, A. S., *A two-phase model for flow of blood in narrow tubes with increased effective viscosity near the wall.* Biorheology, 2001. **38**(5-6): p. 415-28.

55. Rand, R.P., Burton, A. C., *Mechanical Properties of the Red Cell Membrane. I. Membrane Stiffness and Intracellular Pressure.* Biophys J, 1964. **45**: p. 115-35.

56. Evans, E.A., Waugh, R.,Melnik, L., *Elastic area compressibility modulus of red cell membrane.* Biophys J, 1976. **16**(6): p. 585-95.

57. Pfafferott, C., Nash, G. B.,Meiselman, H. J., *Red blood cell deformation in shear flow. Effects of internal and external phase viscosity and of in vivo aging.* Biophys J, 1985. **47**(5): p. 695-704.

58. Lokhandwalla, M., Sturtevant, B., *Mechanical haemolysis in shock wave lithotripsy (SWL): I. Analysis of cell deformation due to SWL flow-fields.* Phys Med Biol, 2001. **46**(2): p. 413-37.